Study of Wind Flow Patterns and Heavy Gas Pollutants Dispersion Under Isolated Building Terrain

Yuyan Fan
Tianjin University
Hong Gao (hgao@tju.edu.cn)
Tianjin University

Research Article

Keywords: Wind tunnel, CFD simulation, Pollutant dispersion, Isolated building, Heavy gas, Safety

Posted Date: May 24th, 2021

DOI: https://doi.org/10.21203/rs.3.rs-498671/v1

Study of wind flow patterns and heavy gas pollutants dispersion under isolated building terrain

Yuyan Fan, Hong Gao*

School of Chemical Engineering and Technology, Tianjin University, Tianjin 300072, PR China

Abstract

Experiment and simulation were used to study the dispersion characteristics of heavy gas pollutants represented by carbon dioxide in isolated building terrain. Wind tunnel experiment and laser particle tracing technology were used to characterize the features of wind flow and the dispersion of pollutants. The influences of the distance from the building to the release source and the size of the building were explored. The results show that the height of the building has a significant effect on the wind speed and turbulence intensity on the windward and leeward sides of the building, and the side width of the building has a slightly weaker effect. The area of the recirculation region on the leeward side of the building and the barrier effect on pollutants are dominated by the windward area of the building, that is, the larger the windward area, the larger the recirculation region and the lower the concentration of pollutants on the leeward side. At the same time, the decline rate of pollutants on the windward side increases with the increase of the windward area. The heavy gas pollutants tend to spread around the building side with the wind flow, unless the distance from the building to the source is too short or the building is too long. And when the pollutants climb to the top of the building, the dispersion of them will slows down as the width of the building side increases. The RNG k-ε model was used for simulation to provide a visible result for wind flow, and its applicability and accuracy were verified.

Keywords: Wind tunnel, CFD simulation, Pollutant dispersion, Isolated building, Heavy gas, Safety

* Corresponding author:
Email: hgao@tju.edu.cn;
Tel.: +86-22-27408399

Introduction

Fluid flow around an obstacle with sharp edges has various flow patterns, so it is extremely unstable (Jiang and Yoshie 2020). Predicting and understanding the characteristics of these flows is of great significance for evaluating wind loads and pollutant dispersion processes in wind engineering. Du (2009) conducted a simulation analysis on 5 simple layout forms of high-rise buildings, studied the wind characteristics under various building layout combinations, and obtained the differences in their impacts. Zhang et al. (2015) combined the computational fluid dynamics (CFD) method and structural modal analysis to numerically study the wind-induced vibration of high-rise building model, and restored several important vortex structures around the building successfully. Tan et al. (2018a, b, 2019) simulated the dispersion of carbon dioxide gas in two typical urban topographies of street canyons and crossroads through wind tunnel experiments and CFD simulation, indicating that under the influence of this type of flows, dangerous wind speeds exist near the source and can make the pollutants reach the maximum concentration, and the influence of the roof shape on the wind field and the dispersion of pollutants was discussed. Mu et al. (2016, 2017) used SF_6 to simulate the dispersion of pollutants in a typical apartment layout, and the results showed that the distribution of wind has a major impact on the cross-layer dispersion of pollutants inside the building, rather than the gravity effect of the gas. Liu et al. (2018) used small field experiments to simulate the leakage of natural gas pipelines near buildings, and observed obvious Coanda effect, which means the fluid has a tendency to flow with the surface of an obstacle, and they suggested to consider this when determining the safe distance between natural gas pipelines and buildings.

Isolated building is a simple but typical terrain, and the wind flow around it contains a variety of basic flow patterns, such as horseshoe vortex, strong separation, vortex shedding and recirculation, etc., which is a good research case. Researchers have been worked on the flow-field around different ground mounted buildings and

bluff bodies, such as the rectangular building (Gorlé et al. 2010), the rooftop stack (Huang et al. 2021) and some complex terrains (Longo et al. 2020a; Balogh et al. 2012) Generally, wind perturbations, recirculation and turbulence caused by buildings affect the distribution of pollutants around them (Li and Stathopoulos 1997; Yi et al. 2020; Longo et al. 2020b). Therefore, if pollutants are discharged near isolated obstacles, their concentration distribution will be strongly affected. Tominaga and Stathopoulos (2010,2017) studied the applicability of several different models for simulating the flow around isolated cubic buildings, and explored the influence of unstable large-scale fluctuations on the dispersion of pollutants around buildings. The results show that the applicability of the model largely depends on the reduction of the wind flow and the location of the release source. Gousseau et al. (2011) studied the convective and turbulent mass fluxes around an isolated building under the two simulation methods of solving the Reynolds-averaged Navier-Stokes (RANS) equations and Large-Eddy Simulation (LES). They found that the accuracy of concentration simulation is affected by the reduction degree of the surrounding flow. Zhang et al. (2016) developed a miniature urban air pollution dispersion simulation model based on wind tunnel experimental data, including a diagnostic wind field model and a random-walk air pollutant dispersion model, and the rapid calculation of pollutant dispersion around isolated buildings is realized.

According to the relative specific gravity with air, gas can be divided into light gas, neutral gas and heavy gas. Ohba et al. (2004) explored the dispersion patterns of light, neutral and heavy gases with obstacles through experiments and simulations. They found that the dispersion of heavy gases is closer to the form of water flow than the other two gases, which covered the surface of obstacles when it dispersed. Xing et al. (2013) conducted a reduced-scale field experiment for carbon dioxide and found that the gravity effect of the gas near the source was obvious, and cloud accumulation and collapse occurred. Owing to the higher density and slower dispersion rate (Deaves 1992), the height of the heavy gases' plume is generally lower, so they are more susceptible to the impact of various buildings and have greater harm to human health. Therefore, the study of heavy gas dispersion has always been the focus of related

research. Tauseef et al. (2011) used the CFD method to simulate the heavy gas dispersion with obstacles, and obtained the concentration fluctuations caused by gravity collapse. Alakalabi and Liu (2019) studied the dispersion of heavy gas in the atmosphere under the action of wind through CFD, observed the stable double peaks of the heavy gas concentration in the downstream area, and explored the distribution of heavy gas clouds under four obstacles situation. Fiates et al. (2016) used methane and carbon dioxide as reference gases to carry out a series of CFD simulations of heavy gas dispersion. During the study, the heavy gas cloud released upwards showed a clear parabolic trajectory under the influence of gravity. The literature also pointed out that owing to the existence of the probe device, the accuracy of the experimental concentration measurement was affected.

In this study, a wind tunnel experiment was carried out with laser particle tracing technology. The flow patterns of heavy gas represented by carbon dioxide under the isolated building terrain was explored, and the influence of the inner measuring devices on the accuracy of the experimental results was avoided. At the same time, the impact of the change of the distance between building and the source as well as the change of the size of buildings on the wind field and the dispersion of heavy gas pollutants was investigated. Moreover, the feasibility of the application of the RNG k-ε model in similar scenarios was verified. It also laid the foundation for the subsequent study of the flow and dispersion of heavy gas in a complex urban environment.

Experiment

The overall experimental device is shown in Figure 1, which is mainly composed of the wind tunnel experimental devices and the concentration display system.

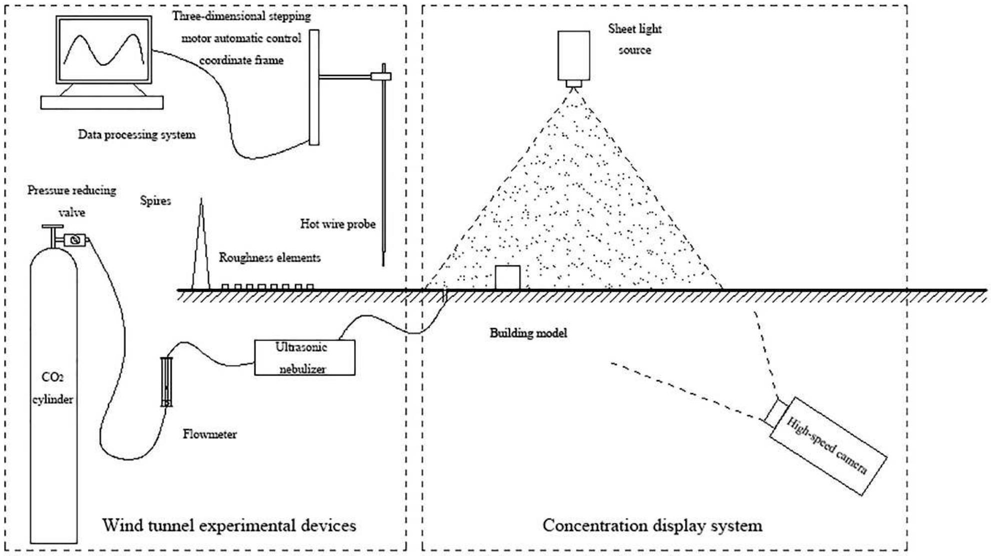

Figure 1. Experimental devices.

The wind tunnel experimental devices

The equipment used in the experiment is the wooden structure TULTWT direct-flow wind tunnel of Tianjin University Fluid Mechanics Laboratory, with a total length of 16.5 m, a maximum width of 1.64 m. The total length of the experimental section is 4.5 m, with a cross-sectional size of 0.35 m×0.45 m. The wind tunnel can achieve continuous speed regulation within the range of 0.5 m/s-41 m/s wind speed. Based on the wind tunnel size, a scaled model was designed for research at a geometric scale of 1:400, and the overall experimental space is 2.5 m×0.35 m×0.45 m. The release source was located at the midline position 1 m after the inlet of the experimental section, with a diameter of 0.005 m. Wedges and rough elements were arranged at the front of the experimental section to simulate the real urban wind profile. The experimental wind profile was measured by the IFA300 constant temperature hot wire anemometer with a three-dimensional stepper motor automatic control frame. 40 sampling points were set with sampling frequency of 20000 Hz and sampling time of 13.12 s to ensure the accuracy of wind speed measurement. According to experimental measurement, the thickness of the boundary layer exceeded 0.25 m. The

height z_0 of the reference point, which is not affected by the building, was selected as 0.1 m, and the wind speed at z_0 was measured as the characteristic wind speed u_0 (=1.3731m/s). After fitting, the wind of the experiment conforms to the power law profile:

$$u = u_0 \left(\frac{z}{z_0} \right)^{\alpha} \tag{1}$$

where z_0 is the height of the reference point, u_0 is the corresponding speed at that height, α is the wind profile index, and its fitted value is 0.24. The wind profile index is related to atmospheric stability and terrain conditions. The "Technical Methods for Establishing Local Air Pollutant Emission Standards (GB/T3840-1991)" (1991) gives a series of index reference values under different atmospheric stability and terrain conditions, as shown in Table 1. The experimental wind speed data and fitting curve are presented in Figure 2, and the results conform to the level of atmospheric stability between C and D of the urban boundary layer.

Table 1 Wind profile index α under different atmospheric stability conditions

	A	B	C	D	E、F
Urban	0.10	0.15	0.20	0.25	0.30
Country	0.07	0.07	0.10	0.15	0.25

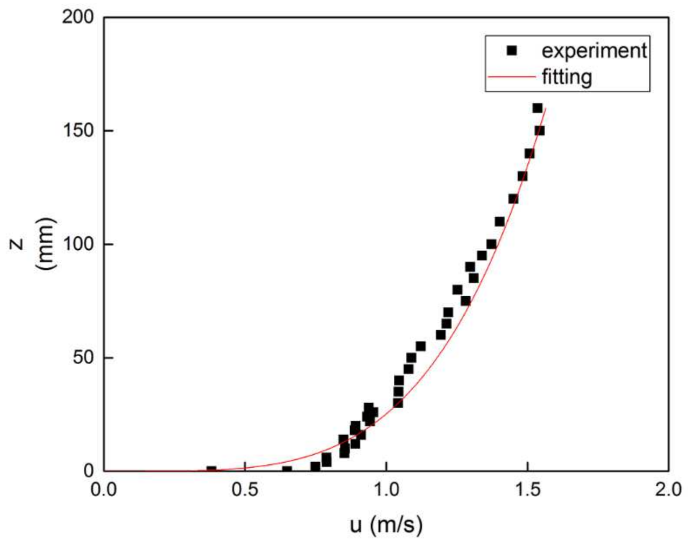

Figure 2. Experimental wind speed and fitting result.

Building models used in the experiment were made from organic glass, seven kinds of cases were considered, including a normal building and six other buildings with changed size. The specific model dimensions are shown in Table 2. Every model was placed 0.06 m downstream of the release source during the experiment, that is, the height of the two normal buildings. Carbon dioxide with a purity of 99.99% was released from the gas cylinder through a pressure reducing valve and a flowmeter. The range of the flowmeter was 2 L/min, the accuracy was 0.1 L/min, and the carbon dioxide release rate was 1.5 L/min.

Table 2 Configuration of experiment models

Configuration	Building Size (L×W×H)
Case 1 (Normal building)	5 cm×3 cm×3 cm
Case 2 (Wide building)	5 cm×5 cm×3 cm
Case 3 (Thin building)	5 cm×1 cm×3 cm
Case 4 (Long building)	9 cm×3 cm×3 cm
Case 5 (Short building)	3 cm×3 cm×3 cm
Case 6 (High building)	5 cm×3 cm×5 cm
Case 7 (Low building)	5 cm×3 cm×1 cm

The concentration display system

The laser particle tracing technology was used to display the concentration distribution during the experiment, and the pure water was atomized into particles using an ultrasonic atomizer with a diameter of less than 9 μm, which was sprayed with carbon dioxide. The cross-section to be observed was irradiated by the laser emitting sheet light and taken with a high-speed camera. The NanoSense series MKIII high-speed camera was used with a shooting frequency of 10 Hz and continuously shot for 20 s. Figure 3(a) shows the image of the instantaneous concentration field

taken by the camera, and Figure 3(b) shows the time-averaged concentration field image after processing. The results are all grayscale images. In the pollutant dispersion experiment, it is considered that the tracer particles meet the uncorrelated single scattering (the dispersion in engineering generally meets this condition). Thus, the intensity of the particle scattered light at a certain position is proportional to the particle concentration for far-field scattering (Luo 2008). As shown in the Figure 3, the concentration at 0.005 m above the source was selected as the reference C_0 for the volume concentration of carbon dioxide, and the concentration at other locations was dimensionless processed, namely:

$$C^* = \frac{C}{C_0} = \frac{I}{I_0} \tag{2}$$

where C^* is the dimensionless carbon dioxide concentration, C_0 is the carbon dioxide concentration near the source, and I_0 is the light intensity near the source. Through this method, the distribution of carbon dioxide can be obtained without contact, and its flow as well as dispersion patterns can be explored.

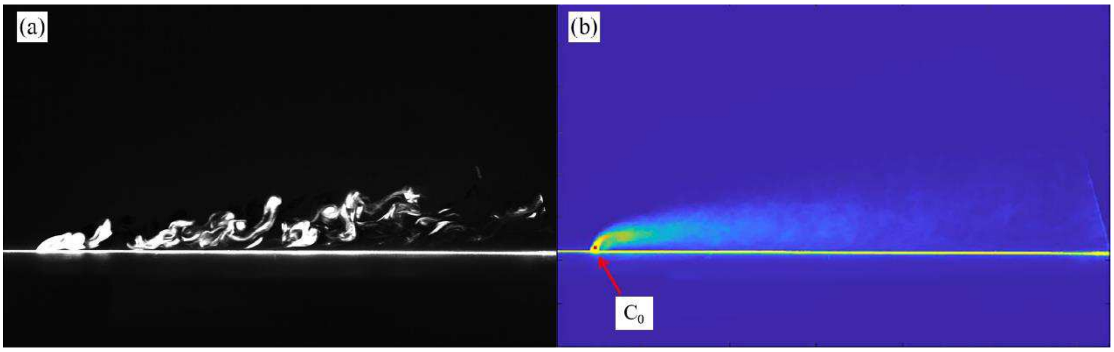

Figure 3. Pictures of (a) the instantaneous concentration field and (b) the time-average concentration field obtained in experiments.

Similarity condition

In order to ensure that the experiment and simulation research have practical significance, the experiment setting needs to satisfy the similarity condition. Tominaga and Stathopoulos (2016) pointed out that while the buoyancy effect of the

released gas cannot be ignored, the consistency of the Froude number Fr has priority over other conditions, and Fr based on air density was selected as the similarity criterion:

$$\mathrm{Fr} = \frac{u_0^{\,2}}{g_0^{'} L} \tag{3}$$

where g_0' is the relative acceleration (=$g(\rho_s$-$\rho_a)/\rho_a$, ρ_s is the density of the releasing gas, ρ_a is the density of air), L is the characteristic length, which was selected as the height of the reference point in this study. According to the principle of equal similarity criterion, the ratio of the speed input in the experiment and numerical simulation to the actual field speed is 1:20. In addition, the experiment needs to ensure the independence of Reynolds number. The building Reynolds number was selected as the criterion, and its reference critical value is 2.1×10^3 (Cui et al. 2017; Ohba 1989):

$$\mathrm{Re_H} = (\frac{u_H H}{\nu}) \tag{4}$$

where H is the height of the normal building, u_H is the wind speed at H, and ν is the movement viscosity of air. After calculation, the building Reynolds number during the experiment is 2112.16, which is greater than its critical value.

Numerical simulation

Domain and mesh

The simulation domain was established according to the size of the wind tunnel. As shown in Figure 4, the building model is located at the midline 2 H downstream of the source, and the lateral length between the building to the boundary is 5 H. The downstream length of the domain is 24 H, and the height is 15 H. The inlet and the source were set as velocity-inlet, and the outlet was set as outflow. The building and the ground were set as wall with the standard wall functions, while the other boundaries were symmetrical boundaries. The ICEM non-structural tetrahedral grid was selected to mesh the model, and the ground, buildings, and the vicinity of the source were refined. The results of Case 1 were selected to verify grid sensitivity, as

shown in Figure 5, three different meshes were set to ensure the independence of the solution from the grid size. The number of cells is 1608513, 2521130 and 6073188 respectively. The difference between the latter two is very small. Considering the computational effort and accuracy, the grid of 2521130 cells was selected. And with the same condition, the number of cells in each case exceeded 2.5 million.

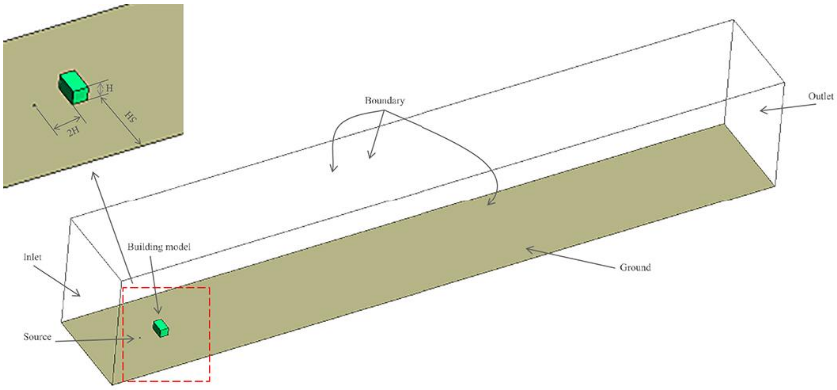

Figure 4. Domain and boundary of numerical simulation.

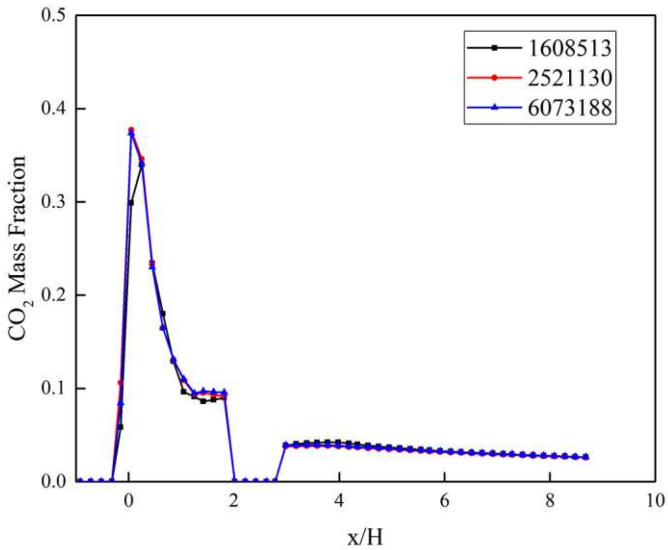

Figure 5. Grid independent verification.

Turbulence model

The Fluent software contains a variety of turbulence models for different situations.

The RNG k-ε model was selected for calculation in this study. Compared with the standard k-ε model, the RNG k-ε model improves the prediction ability of turbulent vortices and the prediction accuracy of near-wall flow (Mirzaei et al. 2019). Moreover, it is also superior in low-speed flow and the reduction of flow pattern details (Tong et al. 2013), which is in good agreement with the experimental results. Therefore, the RNG k-ε model is widely used (Mu 2016, 2017; Tominaga and Stathopoulos 2017; Liu et al. 2017; Zhang et al. 2005; Tan et al. 2017).

Evaluation criteria

Some statistical performance indicators were selected to verify the effectiveness of the simulation, including the geometric mean bias (MG), the geometric variance (VG) and the fraction of predictions within a factor of two of observations (FAC2) (Chang and Hanna 2005), as follows:

$$\mathrm{MG} = \exp(\overline{\ln C_o} - \overline{\ln C_p}) \tag{5}$$

$$\mathrm{VG} = \exp[\overline{(\ln C_o - \ln C_p)^2}] \tag{6}$$

$$\mathrm{FAC2} = \text{fraction of data that satisfy } 0.5 \le \frac{C_p}{C_o} \le 2.0 \tag{7}$$

where C_o is the pollutant concentration observed, C_p is the pollutant concentration predicted by simulation. The ideal model would generate MG, VG and FAC2=1.0. However, this ideal heavy gas model does not exist due to random atmospheric processes. Therefore, a suitable standards to evaluate the statistical performance of the model is crucial. According to Chang and Hanna (2005), $0.7 < \mathrm{MG} < 1.3$, $\mathrm{VG} < 4$, $0.5 < \mathrm{FAC2} < 1$ can be acceptable. The simulation and experimental results of Case 1 were selected as the verification of the model reliability. Limited by the experimental conditions, the gas concentration at the leeward of the building was too low to be accurately displayed by the grayscale map. Therefore, the section of the release source to the building (x/H=0-2) was selected as the key observation area, and statistical performance indicators were calculated by the data of it. As shown in Figure 6, the

results are in good agreement. The truncated part of the curve in the figure is the location of the building in the grayscale map, and the brightness is severely affected by the building. Thus, the part of the data has been deleted.

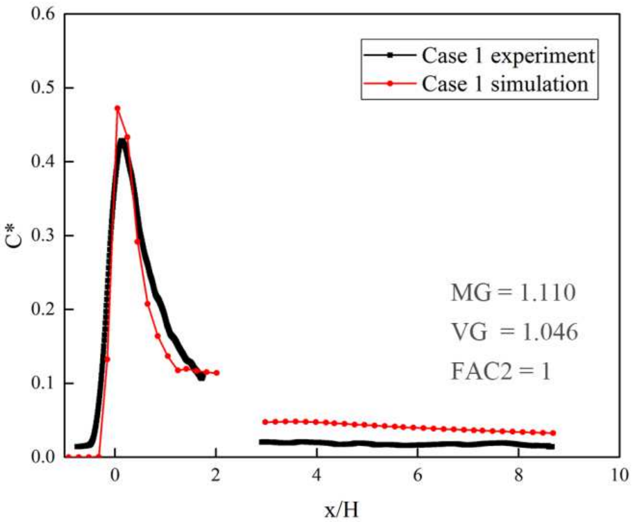

Figure 6. Comparison of simulation and experimental results for Case 1.

Results and discussion

In order to facilitate the analysis of the results of experiment and simulation, different monitoring lines are selected. As shown in Figure 7, line 1 and line 2 are wind speed monitoring locations, which are located at 1 H before and after the building to monitor the wind distribution in the vicinity of the building. Line 3 and line 4 are the concentration monitoring locations, located at the height of 0.5 H and 1.5 H in the center plane to monitor the impact of the building on the dispersion of pollutants.

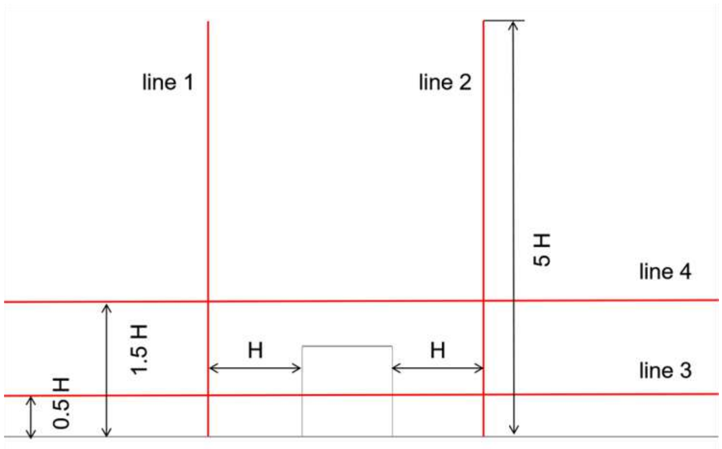

Figure 7. Monitoring lines for wind speed (line 1 and line 2) and pollutant concentration (line 3 and line 4).

Wind flow

Figure 8(a) and (b) respectively show the distribution of wind speed and turbulence intensity at line 1 and line 2 in Case 1, and the situation with no building exist was compared to investigate the influence of the building on the wind flow. Obviously, the impact of buildings on the wind field on the leeward side is greater than that on the windward side. In terms of wind speed, the affected areas before and after the building are concentrated below the height of the building, H. Compared with the case of no building, the wind speed on the windward side decreases slightly from height H, while the wind speed on the leeward side decreases sharply, and even reverse wind speed appears. The turbulence intensity begins to increase at about 1/3 H on the windward side of the building, and reaches the maximum when it is close to the ground, indicating that the flow turbulence degree below 1/3 H is higher. On the leeward side, the turbulence intensity reaches its maximum at the height H.

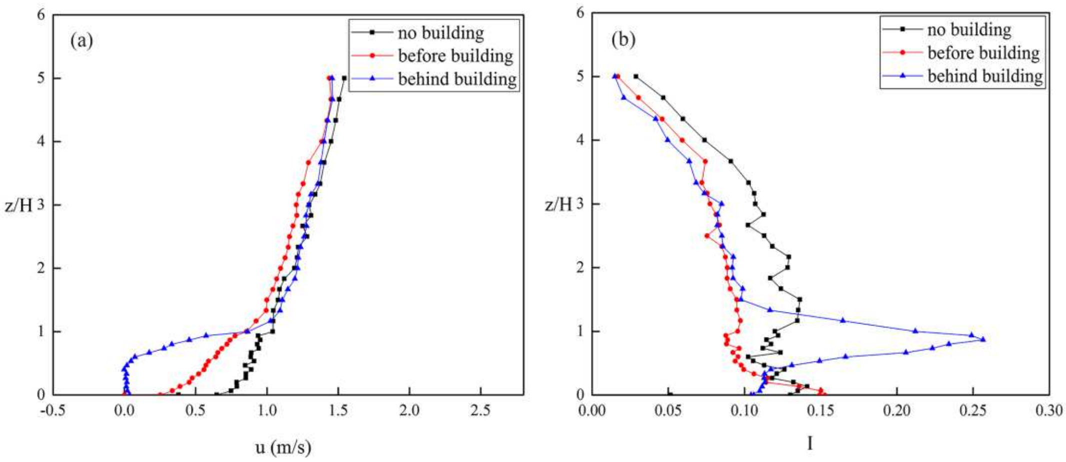

Figure 8. Distribution of (a) wind speed and (b) turbulence intensity at line 1 and line 2 in Case 1.

Figure 9(a) and (b) display the wind speed at line 1 and line 2 of the building under different conditions, while (c) and (d) show the turbulence intensity, respectively, which are similar to those of normal building (Case 1). Figure 9(a) clearly shows that the height of the building has the greatest influence on the distribution of wind speed in front of the building. The wind speed overlap highly in the area without building influence (above 3 H), and the influenced range is obviously lager (less) than other cases in Case 6 (Case 7) where the building height changes. In addition, as shown in the enlarged image, the windward area of the building also has a certain influence. In Case 4, owing to the larger windward area, the wind speed decreases greater, while Case 5 is just the opposite. The wind speed distribution of Case 1-3 with the same windward area is very close. Similarly, building height in Figure 9(b) is the most effective factor. The difference is that the width of the side of the building has a significant impact. The wind speed distribution in the Case 3 changes significantly with the thinnest building, which is higher than that in other cases except Case 6. In Figure 9(c), the turbulence intensity distribution in front of buildings overlaps extremely highly, especially above the height H. Moreover, the turbulence intensity increases are concentrated at 1/2-1/3 H. The turbulence distribution on the leeward side of the building in Figure 9(d) is similar to that in Figure 8(b), and the peak position obviously depends on the height of buildings. Similar to Figure 9(b), except

for Case 6, Case 3 has the highest turbulence intensity, although its windward area is the same as Case 1 and Case 2, while Case 2 has the lowest turbulence intensity among the three.

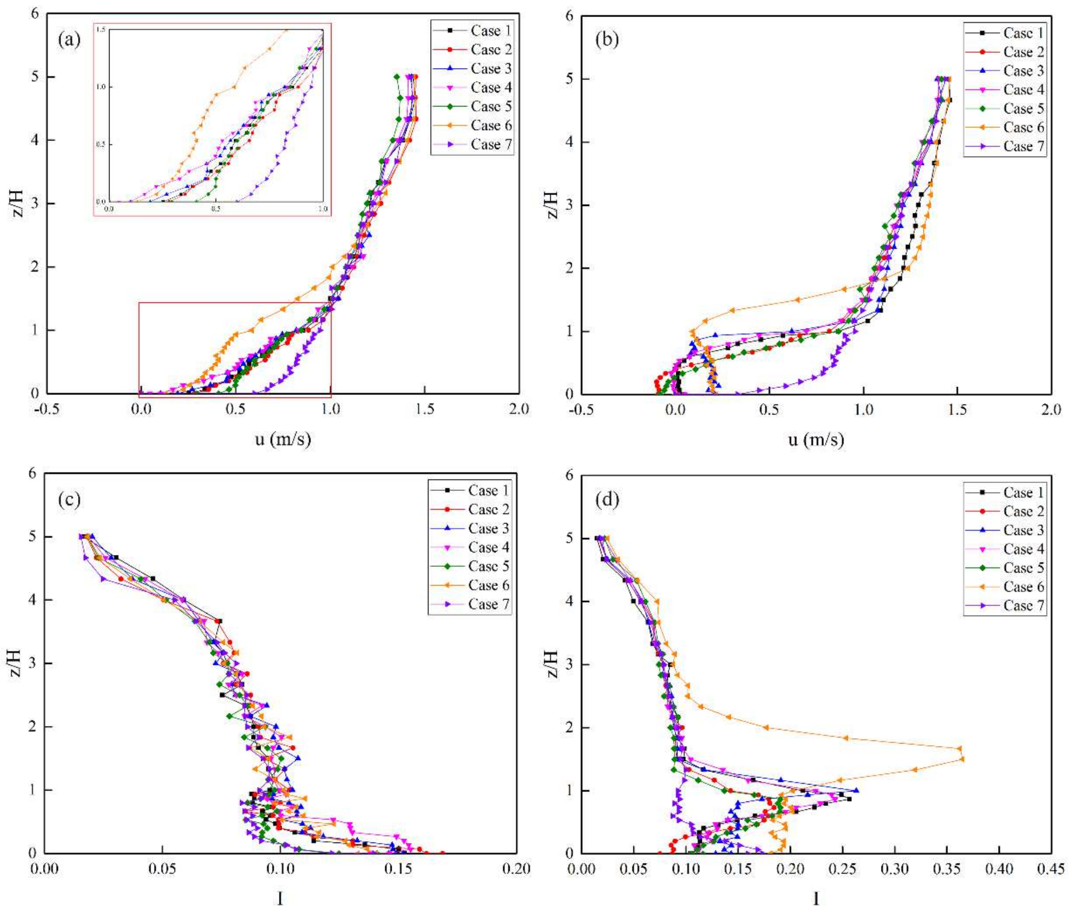

Figure 9. The wind speed (a, b) and the turbulence intensity (c, d) at line 1 and line 2 of the building under different conditions.

Figure 10 presents the time-averaged streamline and pressure contour of the horizontal plane of the ground (z=0) obtained by simulation. According to the method proposed by Jiang et al. (2020), the two main curves in the figure are marked as *a* and *b*. Curve *a* is the separation curve formed by the mainstream encountering obstacles, and curve *b* surrounds the recirculation region behind the obstacle. All the cases have similar streamlines except for Case 7. The curve *a* in Case 7 is not obvious, and it overlaps with curve *b* from the side of the building. Four characteristic lengths are defined to characterize the shape of the ground flow: d_a is the flow distance from the

windward side of the building to curve *a*, d_b is the flow distance from the leeward side of the building to curve *b*, while W_a and W_b are the lateral width of curves *a* and *b* respectively. Table 3 shows the normalized results of the four characteristic lengths in Case 1-7 with respect to the building height H. When the windward area of the building is the same (Case 1-3), the distance d_a of curve *a* is really close, and its width W_a is the same in Case 1 and Case 2, but a little larger in Case 3; while the distance d_b and width W_b of curve *b* obviously increase as the building width decreases, that is, the area of the recirculation region behind the leeward side (defined as $d_b/H \times W_b/H$) increases with the decrease of the building width, which is consistent with the results obtained by the LES method (Jiang and Yoshie 2020). When the windward area of the building changes (Case 1 and Case 4-7), the shape of curve *b* is dominated by the change. As the windward area decreases, the recirculation region on the leeward side also decreases (Case 7<Case 5<Case 1<Case 6<Case 4). The distribution of curve *a* is more complicated. When the height of the windward area is constant (Case 1, Case 4 and Case 5), d_a and W_a increase with the length; and when the length of the windward area is constant (Case 1, Case 6 and Case 7), they increase with the height; finally, when the length and height change at the same time, no obvious regularity is observed.

The pressure contour on the ground in different cases shown in Figure 10 is similar. Two high-pressure zones are mainly present, including the middle of the windward side of the building and the end of the recirculation region. The low-pressure area is concentrated in the side wall of the building and the interior of the recirculation region. This type of area is prone to vortex shedding and reattachment, and the flow in the area is highly turbulent. In comparison, Case 7 has the smallest overall volume of the building, so it has the weakest impact on the wind field. In Case 4, the area of the low pressure surrounded by curve *b* is larger than other cases, but the high pressure area before and after the building is not obvious. It is speculated that the long windward side has the effect of dispersing pressure, and the recirculation of the leeward side is moderate, the pressure on the ground produced by the fluid reattaching is small.

Table 3 Normalized results of the four characteristic lengths in Case 1-7

Configuration	d_a/H	d_b/H	W_a/H	W_b/H	$d_b/H \times W_b/H$
Case 1	1.289	3.518	4.171	2.640	9.288
Case 2	1.289	2.831	4.171	2.524	7.145
Case 3	1.277	4.181	4.547	2.832	11.841
Case 4	1.494	5.819	5.665	4.586	26.686
Case 5	0.940	2.277	3.218	1.724	3.926
Case 6	1.831	5.470	5.723	3.362	18.390
Case 7	0.301	1.410	2.322	2.322	3.274

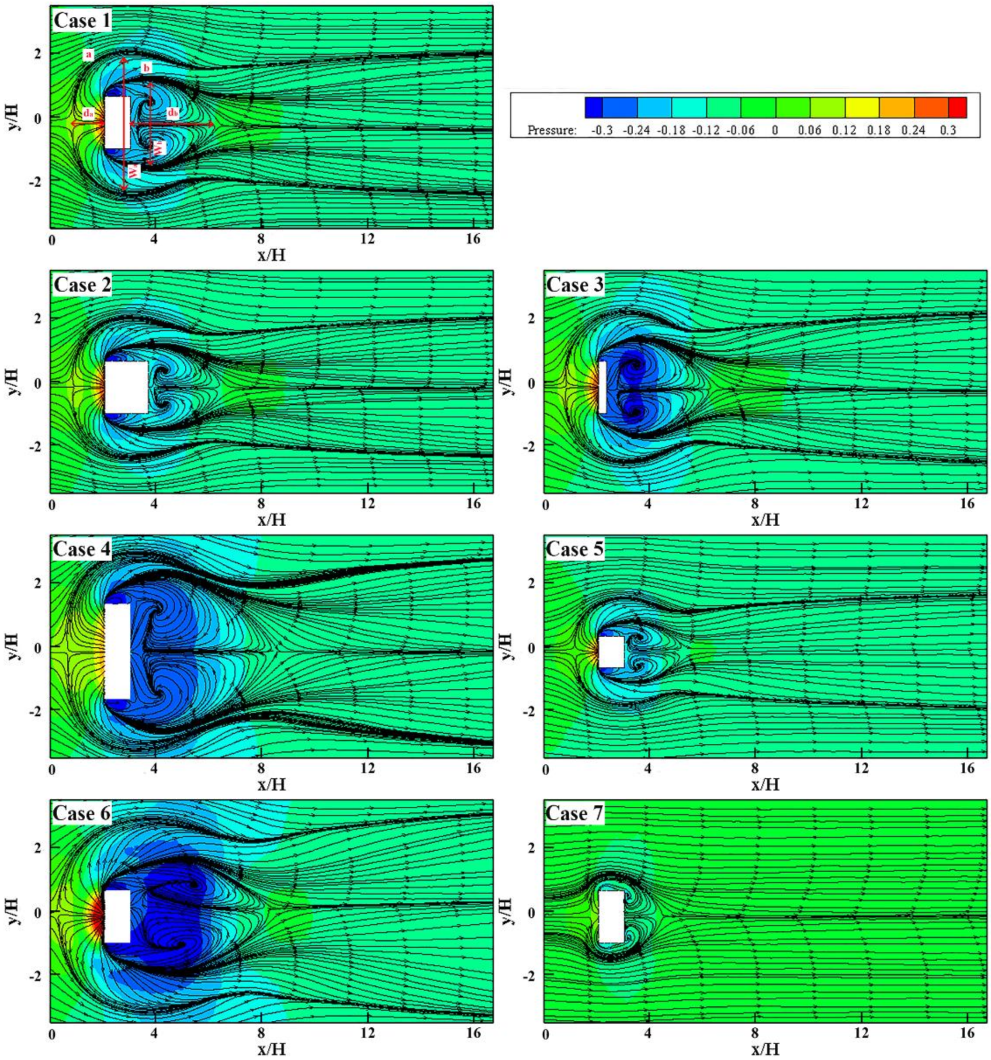

Figure 10. Time-averaged streamline and pressure contour of the horizontal plane of the ground (z=0) obtained by simulation.

Figure 11 and Figure 12 respectively illustrate the time-averaged streamline and flow velocity contour of the horizontal plane (z/H=0.5) and vertical plane in the middle of the building (y=0). From the streamline distribution in Figure 11, all cases retain curve *b* (except for Case 7, where the horizontal planet is higher than the building height); curve *a* disappears, indicating that it is produced by the combined effect of the ground and the building, and the reverse flow on the windward side of the building only exists near the ground. The distribution law of the recirculation region enclosed by curve *b* is the same as that of the near-ground flow field. Compared with the shape of the streamline in Figure 10, the expansion stage of curve *b* is no longer obvious, that is, the width W_b is reduced, and the overall state of contraction is shown, no further expansion occurs after away from the building. In the streamline in the vertical plane presented in Figure 12, each case mainly contains two vortices. The vortex on the windward side is located below 2/3 of the height of the building, namely under the “stagnation zone” (Mu et al. 2016). Its core is located at about 1/3 H, which is consistent with the increase in turbulence intensity in Figure 9(c), and its size is obviously affected by the windward area. The core of the leeward side vortex locates near the building top, corresponding to the peak position of the turbulence intensity in Figure 9(d). The generation of the vortex on the windward side causes a reverse flow near the ground. A fluid reattachment point exists outside the recirculation region behind the leeward side, and its distance to the leeward side is d_b, which is controlled by the windward area and the width of the side of the building. The edge of the recirculation region in Case 4 seems smooth, there is no contraction similar to other cases and no obvious vortex core inside. This may be the reason why the high-pressure area on the ground in Case 4 is not obvious.

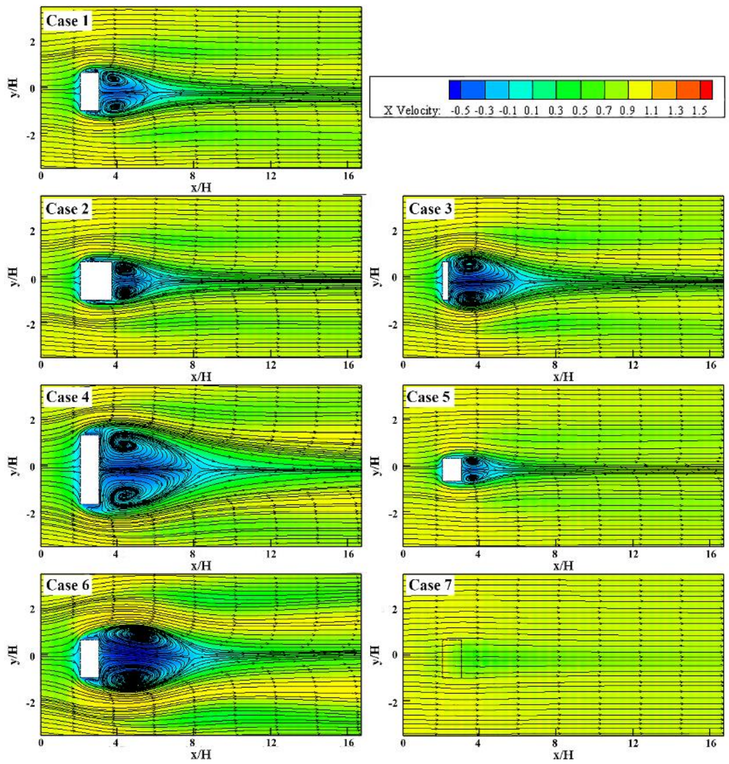

Figure 11. Time-averaged streamline and flow velocity counter of the horizontal plane (z/H=0.5) obtained by simulation.

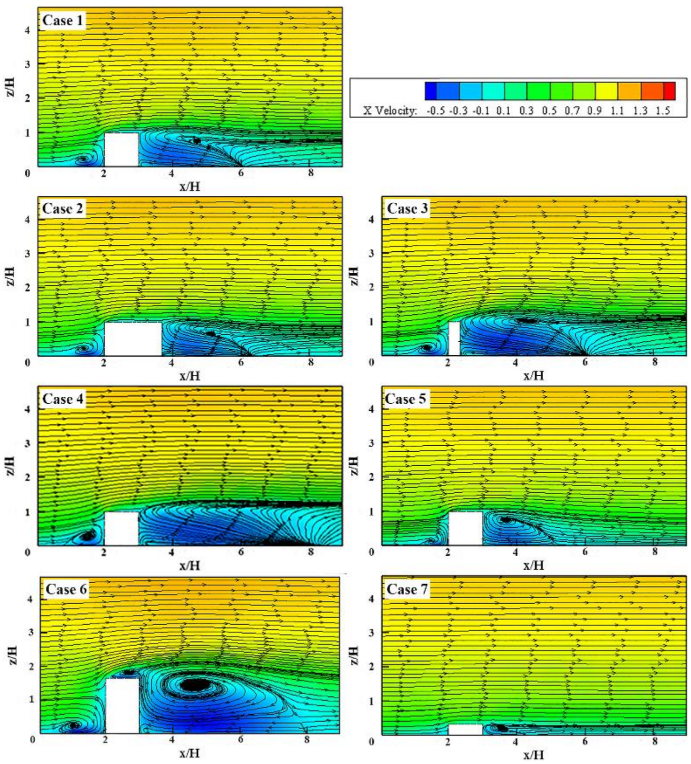

Figure 12. Time-averaged streamline and flow velocity counter of the vertical plane (y=0) in the middle of the building obtained by simulation.

Pollutant concentration

Changes in distance between building and source

Figure 13 shows the results of the experiment that changes the distance between the building and the release source, and the distances are H, 2 H, and 6.5 H, respectively. The experiment without building is used as a comparison. Figure 13 (a) displays the instantaneous concentration field, and (b) displays the time-averaged concentration field. Figure 14 presents the concentration distribution curves at line 3 in the above experiment. The results show that the closer the building is to the source, the greater the barrier to pollutants. When the distance is H, most of the pollutants disperse over the building depends on the initial momentum after release. The dispersion space in front of the building is small, so the peak concentration of this case is the highest and the decline rate is the fastest of the three situations. More pollutants can disperse to the leeward of the building, and the concentration on the leeward side is slightly higher than it in the other two cases. When the distance is 2 H, the pollutants will disperse downwind for a certain distance after release, and the concentration will drop rapidly after encountering the building. Owing to the large free dispersion space, the peak concentration is lower than it of the H distance. As shown in the instantaneous graph, part of pollutants is involved in the vortex near the ground on the windward side of the building and accumulates. Thus, the concentration declines slowly. The building is located at the tail of the visible plume when the distance is 6.5 H, which has the least impact on the dispersion, and the pollutants dispersion is similar to that without buildings.

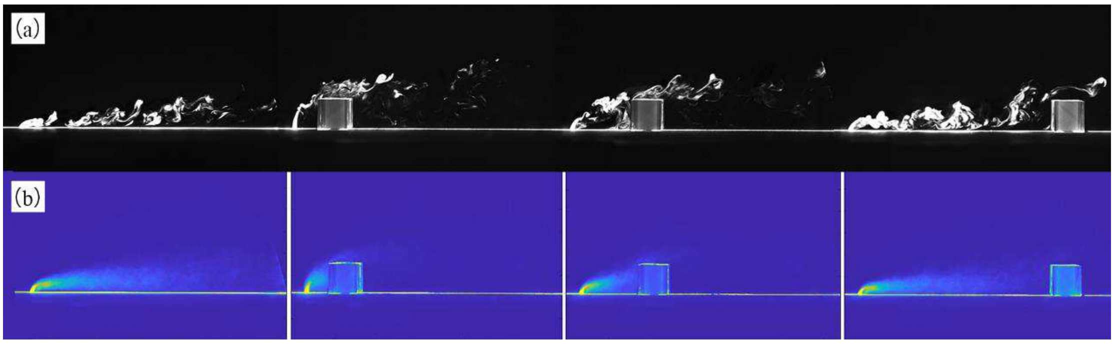

Figure 13. Results of the experiments with different distance between the building and the release source (no building, H, 2 H and 6.5 H): (a) instantaneous concentration field; (b) time-averaged concentration field.

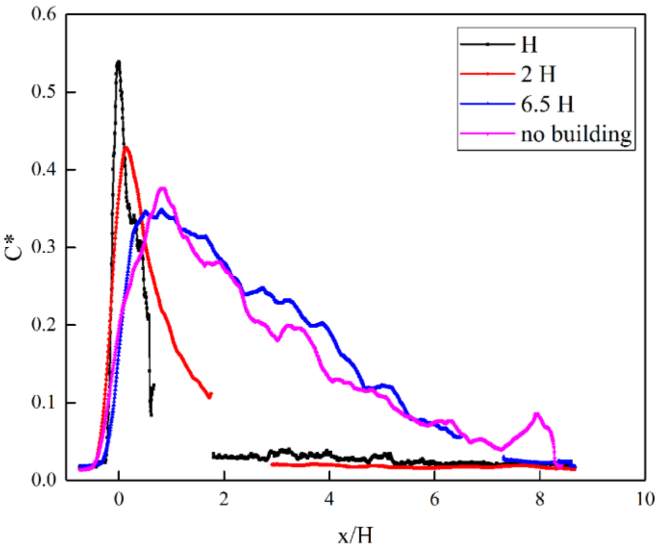

Figure 14. Concentration distribution curves on line 3 of the experiments with different distance between the building and the release source.

Changes in building size

Figure 15 shows the concentration distribution curve of line 3 or line 4 in the experiments with different building size, where (a) shows the results on line 3 where the building width changes (Case 1-3), and (b) shows that on line 4; (c) shows the results on line 3 where the building length changes (Case 1, Case 4 and Case 5), and (d) shows that on line 4; (e) shows the results on line 3 where the building height changes (Case 1, Case 6 and Case 7). The three curves in Figure 15(a) overlap well,

which proves that the change of building width has almost no effect on the concentration curve at line 3 on the windward side, which is similar to the wind field distribution. When the windward side of the building is the same, the wind field and the pollutant distribution in the front of the building tend to be consistent. In Figure 15(b), the peak concentration at the top of the building in the three cases are close, and they are all located above the building ($2<x/H<3$). The width of the peak increases with the building width, indicating that the pollutants are less likely to disperse due to the cushioning effect of the building. In Figure 15(c), as the length of the building increases, peak value of the concentration in front the building increases. However, the position is relatively close. The concentration at the leeward of the short building (Case 7) is higher than the other two cases due to the lateral flow of pollutants. In Figure 15(d), a huge difference exists in the peak concentration values at the top of the building in the three cases. As the length of the building increases, more pollutants disperse over the top of the building. In Case 5, the pollutant concentration is the lowest and the fluctuation range is small, indicating that the heavy gas pollutants tend to flow around horizontally rather than climbing. In Figure 15(e), the higher the building, the greater the barrier to pollutant, and the higher the concentration peak before the building. The concentration distribution of Case 6 and Case 1 on the windward side is similar, and the concentration peak position is very close, while the peak in Case 7 is lower and further from the source. The influence of the building in Case 7 is small, and the concentration is in a continuous decline state, which is close to the free dispersion. The decreasing trend of the concentration before the building increases with the increase in the building height. Considering the situation in Figure 15(c), the downward trend of pollutants on the windward side of the building is affected by the windward area. Case 5 and Case 7 with smaller windward areas have significantly wider peaks of pollutant concentration on the windward side and a slower reduction rates, which may be caused by the influence of wind pressure and backflow.

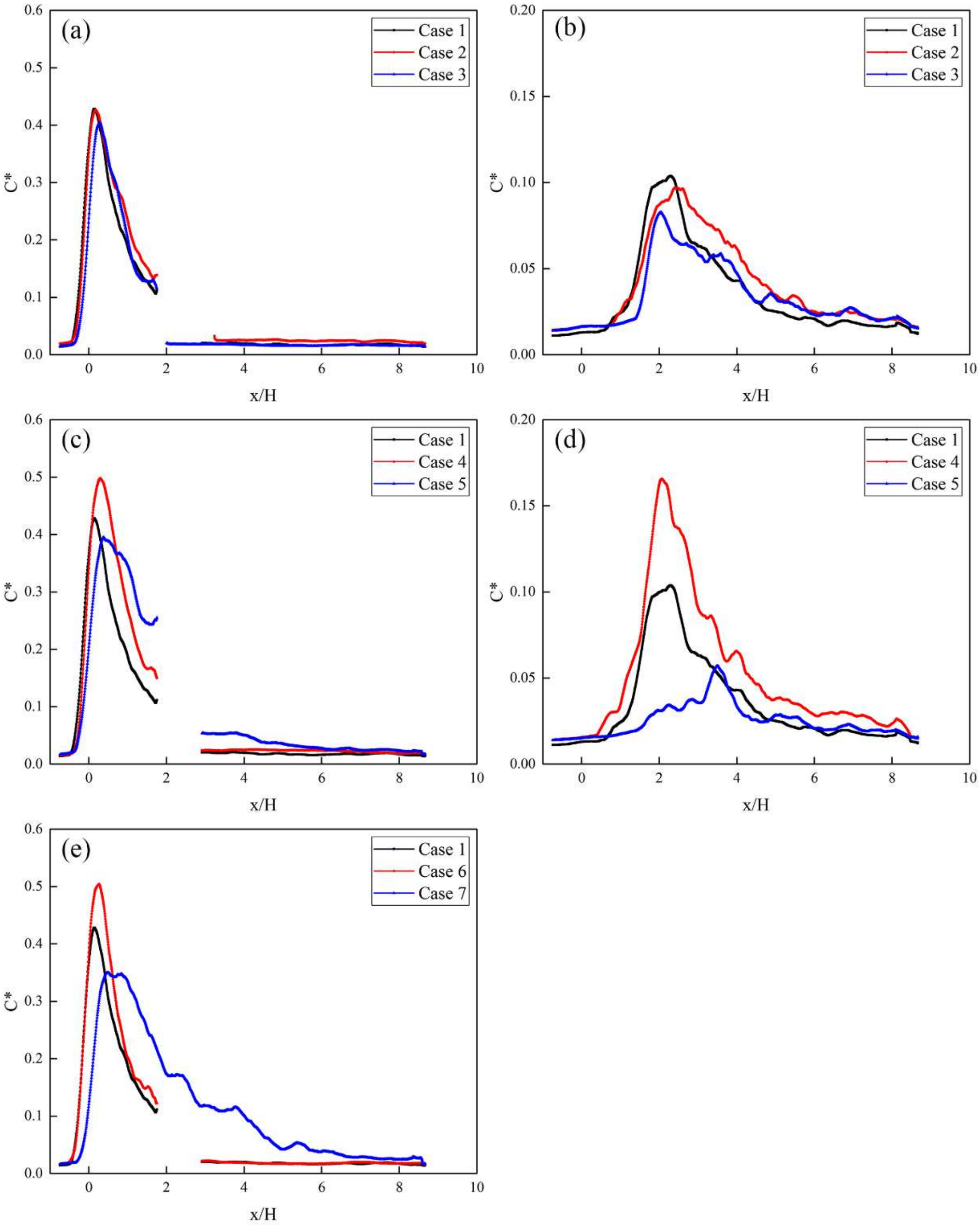

Figure 15. Concentration distribution curve of line 3 (a, c, e) or line 4 (b, d) in the experiments with different building size.

Limited by the experimental conditions, the pollutant concentration on the leeward side of buildings cannot be accurately displayed by the grayscale image. Therefore, the simulation results were selected to analyze the pollutant concentration distribution in the leeward side recirculation region, as shown in Figure 16. The building has a strong barrier effect on pollutants, and the mass fraction of all cases has dropped

below 0.1. The concentration curves are obviously divided into three groups: upper, middle and lower, which depend on the windward area of the building. Case 5 and Case 7, which have the smallest windward area, have the highest pollutant concentration in the recirculation region, Case 1-3 with the same windward area have the middle concentration, and Case 4 and Case 6 with the largest windward area have the lowest concentration. The windward area of the Case 5 is about 2 times of Case 7, but the pollutant concentration of the two is not much different. The results indicates that when the length of the building is short, the lateral flow can promote the further dispersion of pollutants, and barrier effect of the building is weak.

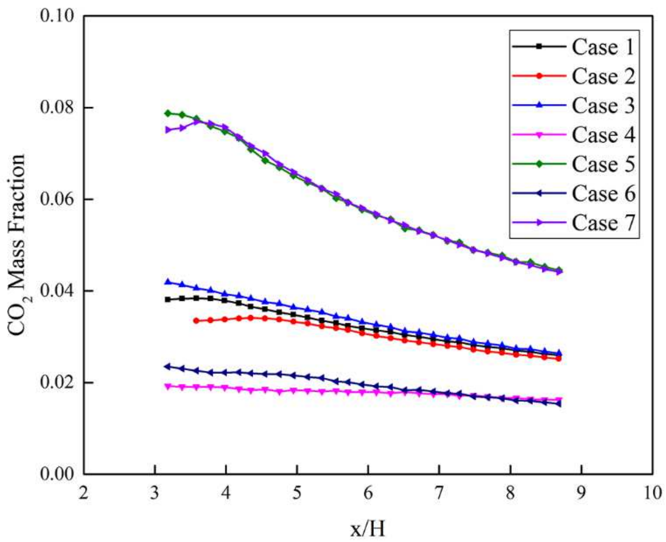

Figure 16. Pollutant concentration distribution on the leeward side obtained by simulation.

Conclusion

Wind tunnel experiments and CFD simulations were used to study the dispersion state of carbon dioxide in the isolated building terrain. The laser particle tracing technology visually displayed the instantaneous and time-averaged concentration distribution of pollutants during the experiment. Therefore, the influence of the internal measuring

device on the results was successfully avoided. Considering the influence of the distance between the isolated building and the source as well as the change of building size on the wind flow and heavy gas dispersion, the main conclusions are as follows:

1. The affected area of wind flow on the windward and leeward sides of isolated buildings is concentrated below the height of the building, which is specifically manifested as a decrease in wind speed and an increase in turbulence intensity. The intensity of turbulence is dominated by the vortex near the building, and its enhanced position is concentrated at the height of 1/3 H (windward side) and H (leeward side). When the windward area is equal, the side width of the building has a significant impact. The narrower the side, the higher the turbulence of the surrounding wind field;

2. The RNG k-ε model can be well adapted to the simulation of similar scenarios, which successfully restored the various fluid flow patterns around isolated buildings and the dispersion state of heavy gas pollutants. The former is close to the results obtained by LES (Jiang and Yoshie 2020), while the latter is consistent with the experimental results. The wind flow on the ground has a complex flow pattern, which mainly includes the main separation stream on the windward side of the building and the flow surrounding the recirculation region on the leeward side. When the windward area is the same, the shape of the main separation stream is approximately the same. When the windward area is different, it is affected differently by the change of building length and height. The area of the recirculation region on the leeward side is dominated by the windward area, which increases with the latter; when the windward area remains the same, the recirculation region increases with the decrease in the building width. The horizontal streamline distribution away from the ground is similar to that of the ground. However, the main separation stream disappears and the back flow area around the building is reduced;

3. The experimental results of the change of the distance between the building and the release source indicate that the shorter the distance, the greater the barrier to pollutants. The increase in the dispersion space in front of the building will slow

down the rate of pollutant concentration decline. Meanwhile, since the heavy gas pollutants tend to disperse close to the ground, the pollutants at a remote location are more likely to be involved in the windward side vortex of the building after they are free from the initial upward momentum;

4. Buildings have a strong barrier effect on pollutants, and the concentration of pollutants on the windward and the leeward sides is huge differently. The area of the windward side of the building affects the dispersion trend of pollutants. When the windward area is the same, the pollutants distribution is similar. Otherwise, the pollutants decline rate of the windward side is slower with a smaller area. Meanwhile, the concentration on the leeward side of the building is dominated by the windward area. The heavy gas pollutants tend to spread around the building side with the flow. Moreover, the increase in the length of the building will force it to climb upwards, significantly increasing the pollutant content on the top of the building. The dispersion of pollutants climbing to the top is affected by the width of the building side, and a larger width will delay the entry of pollutants into the recirculation region, resulting in a reduced rate of pollutants concentration decline.

Authors' contributions All authors contributed to the study conception and design. The first draft of the manuscript was written by Y.F., and all authors commented on previous versions of the manuscript. All authors read and approved the final manuscript.

Funding The work was financially supported by the National Key R&D Program of China (No.2018YFC0808600).

Data availability The datasets used and/or analyzed during the current study are available from the corresponding author on reasonable request.

Declarations

Ethics approval and consent to participate Not applicable.

Consent for publication Not applicable.

Competing interests The authors declare no competing interests.

References

Alakalabi A, Liu W (2019) Numerical Investigation into the effects of obstacles on heavy gas dispersions in the atomsphere. E3S Web of Conferences. 128: 09002. https://doi.org/10.1051/e3sconf/201912809002

Balogh M, Parente A, Benocci C et al (2012) RANS simulation of ABL flow over complex terrains applying an Enhanced k-e model and wall function formulation: Implementation and comparison for fluent and OpenFOAM. J Wind Eng Ind 104-106: 360-368. https://doi.org/10.1016/j.jweia.2012.02.023

Chang JC, Hanna SR (2005) Technical Description and User's Guide for the BOOT Statistical Model Evaluation Software Package, Version 2.0. George Mason University and Harvard School of Public Health, Fairfax, Virginia, USA.

Cui P, Li Z, Tao W (2017) Numerical investigations on re-independence for the turbulent flow and pollutant dispersion under the urban boundary layer with some experimental validations. Int J Heat Mass Transf 106: 422-436. http://dx.doi.org/10.1016/j.ijheatmasstransfer.2016.08.038

Deaves DM (1992) Dense gas dispersion modelling. J Loss Prev Process Ind 5: 219-227. https://doi.org/10.1016/0950-4230 (92)80044-9

Du J (2009) Numerical simulation of wind environment in some typical layout residential district. Dissertation, Hunan University

Fiates J, Santos RRC, Neto FF et al (2016) An alternative CFD tool for gas dispersion

modelling of heavy gas. J Loss Prev Process Ind 44: 583-593. http://dx.doi.org/10.1016/j.jlp.2016.08.002

GB/T 3840-1991, Technical methods for establishing local air pollutant emission standards. National Standard of China.

Gorlé C, Rambaud P, Beeck J (2010) Large eddy simulation of flow and dispersion in the wake of a rectangular building. The Fifth International Symposium on Computational Wind Engineering

Gousseau P, Blocken B, Heijst GJF (2011) CFD simulation of pollutant dispersion around isolated buildings: On the role of convective and turbulent mass fluxes in the prediction accuracy. J Hazard Mater 194: 422-434. https://doi.org/10.1016/j.jhazmat.2011.08.008

Huang YD, Xu N, Ren SQ et al (2021) Numerical investigation of the thermal effect on flow and dispersion of rooftop stack emissions with wind tunnel experimental validations. Environ Sci Pollut R 28: 11618-11636. https://doi.org/10.1007/s11356-020-11304-y

Jiang G, Yoshie R (2020) Side ratio effects on flow and pollutant dispersion around an isolated high-rise building in a turbulent boundary layer. Build Environ 180: 107078. https://doi.org/10.1016/j.buildenv.2020.107078

Li Y, Stathopoulos T (1997) Numerical evaluation of wind-induced dispersion of pollutants around a building. J Wind Eng Ind. Aerod 67&68: 757–766. https://doi.org/10.1016/S0167-6105 (97)00116-5

Liu A, Huang J, Li Z et al (2018) Numerical simulation and experiment on the law of urban natural gas leakage and diffusion for different building layouts. J Nat Gas Sci Eng 54: 1-10. https://doi.org/10.1016/j.jngse.2018.03.006

Liu S, Pan W, Zhang H et al (2017) CFD simulations of wind distribution in an urban community with a full-scale geometrical model. Build Environ 117: 11-23. http://dx.doi.org/10.1016/j.buildenv.2017.02.021

Longo R, Bellemans A, Derudi M et al (2020b) A multi-fidelity framework for the estimation of the turbulent Schmidt number in the simulation of atmospheric dispersion. Build Environ 185: 107066.

https://doi.org/10.1016/j.buildenv.2020.107066

Longo R, Nicastro P, Natalini M et al (2020a) Impact of urban environment on Savonius wind turbine performance: a numerical perspective. Renew Energ 156: 407-422. https://doi.org/10.1016/j.renene.2020.03.101

Luo Q (2008) Wind tunnel experimental study on air pollutant transportation and dispersion for hilly terrain. Dissertation, Tianjin University

Mirzaei Fz, Mirzaei Fs, Kashi E (2019) Turbulence model selection for heavy gases dispersion modeling in topographically complex area. JAFM 12: 1745-1755. https://doi.org/10.29252/jafm.12.06.29685

Mu D, Gao N, Zhu T (2016) Wind tunnel tests of inter-flat pollutant transmission characteristics in a rectangular multi-storey residential building, part A: Effect of wind direction. Build Environ 108: 159-170. http://dx.doi.org/10.1016/j.buildenv.2016.08.032

Mu D, Shu C, Gao N et al (2017) Wind tunnel tests of inter-flat pollutant transmission characteristics in a rectangular multi-storey residential building, part B: Effect of source location. Build Environ 114: 281-292. http://dx.doi.org/10.1016/j.buildenv.2016.12.031

Ohba M (1989) Experimental studies for effects of separated flow on gaseous diffusion around two model buildings. Trans AIJ: J Arch Plan. Environ Eng 406: 21-30. https://doi.org/10.3130/aijax.406.0_21

Ohba R, Kouchi A, Hara T et al (2004) Validation of heavy and light gas dispersion models for the safety analysis of LNG tank. J Loss Prev Process Ind 17: 325-337. https://doi.org/10.1016/j.jlp.2004.06.003

Tan W, Du H, Liu L et al (2017) Experimental and numerical study of ammonia leakage and dispersion in a food factory. J Loss Prev Process Ind 47: 129-139. http://dx.doi.org/10.1016/j.jlp.2017.03.005

Tan W, Li C, Wang K et al (2018a) Dispersion of carbon dioxide plume in street canyons. Process Saf Environ 116: 235-242. https://doi.org/10.1016/j.psep.2018.01.020

Tan W, Li C, Wang K et al (2019) Geometric effect of buildings on the dispersion of

carbon dioxide cloud in idealized urban street canyons. Process Saf Environ 122: 271-280. https://doi.org/10.1016/j.psep.2018.12.020

Tan W, Wang K, Li C et al (2018b) Experimental and numerical study on the dispersion of heavy gases in urban environments. Process Saf Environ 116: 640-653. https://doi.org/10.1016/j.psep.2018.03.027

Tauseef SM, Rashtchian D, Abbasi SA (2011) CFD-based simulation of dense gas dispersion in presence of obstacles. J Loss Prev Process Ind 24: 371-376. https://doi.org/10.1016/j.jlp.201 1.01.014

Tominaga Y, Stathopoulos T (2010) Numerical simulation of dispersion around an isolated cubic building: Model evaluation of RANS and LES. Build Environ 45: 2231-2239. https://doi.org/10.1016/j.buildenv.2010.04.004

Tominaga Y, Stathopoulos T (2016) Ten questions concerning modeling of near-field pollutant dispersion in the built environment. Build Environ 105: 390-402. http://dx.doi.org/10.1016/j.buildenv.2016.06.027

Tominaga Y, Stathopoulos T (2017) Steady and unsteady RANS simulations of pollutant dispersion around isolated cubical buildings: Effect of large-scale fluctuations on the concentration field. J Wind Eng Ind. Aerod 165: 23-33. http://dx.doi.org/10.1016/j.jweia.2017.02.001

Tong G, Zhang G, Christopher DM et al (2013) Evaluation of turbulence models to predict airflow and ammonia concentrations in a scale model swine building enclosure. Comput Fluids 71: 240-249. http://dx.doi.org/10.1016/j.compfluid.2012.10.020

Xing J, Liu Z, Huang P et al (2013) Experimental and numerical study of the dispersion of carbon dioxide plume. J Hazard Mater 256-257: 40-48. http://dx.doi.org/10.1016/j.jhazmat.2013.03.066

Yi Q, Zhang G, Amon B et al (2020) Modelling air change rate of naturally ventilated dairy buildings using response surface methodology and numerical simulation. Build Simul 14: 827-839. https://doi.org/10.1007/s12273-020-0697-z

Zhang N, Du Y, Miao S (2016) A Microscale Model for Air Pollutant Dispersion Simulation in Urban Areas: Presentation of the Model and Performance over a

Single Building. Adv Atmos Sci 33: 184-192. http://10.1007/s00376-015-5152-1

Zhang A, Gao C, Zhang L (2005) Numerical simulation of the wind field around different building arrangements. J Wind Eng Ind. Aerod 93: 891-904. https://doi.org/10.1016/j.jweia.2005.09.001

Zhang Y, Habashi WG, Khurram RA (2015) Predicting wind-induced vibrations of high-rise buildings using unsteady CFD and modal analysis. J Wind Eng Ind Aerod 136: 165-179. http://dx.doi.org/10.1016/j.jweia.2014.11.008

Figures

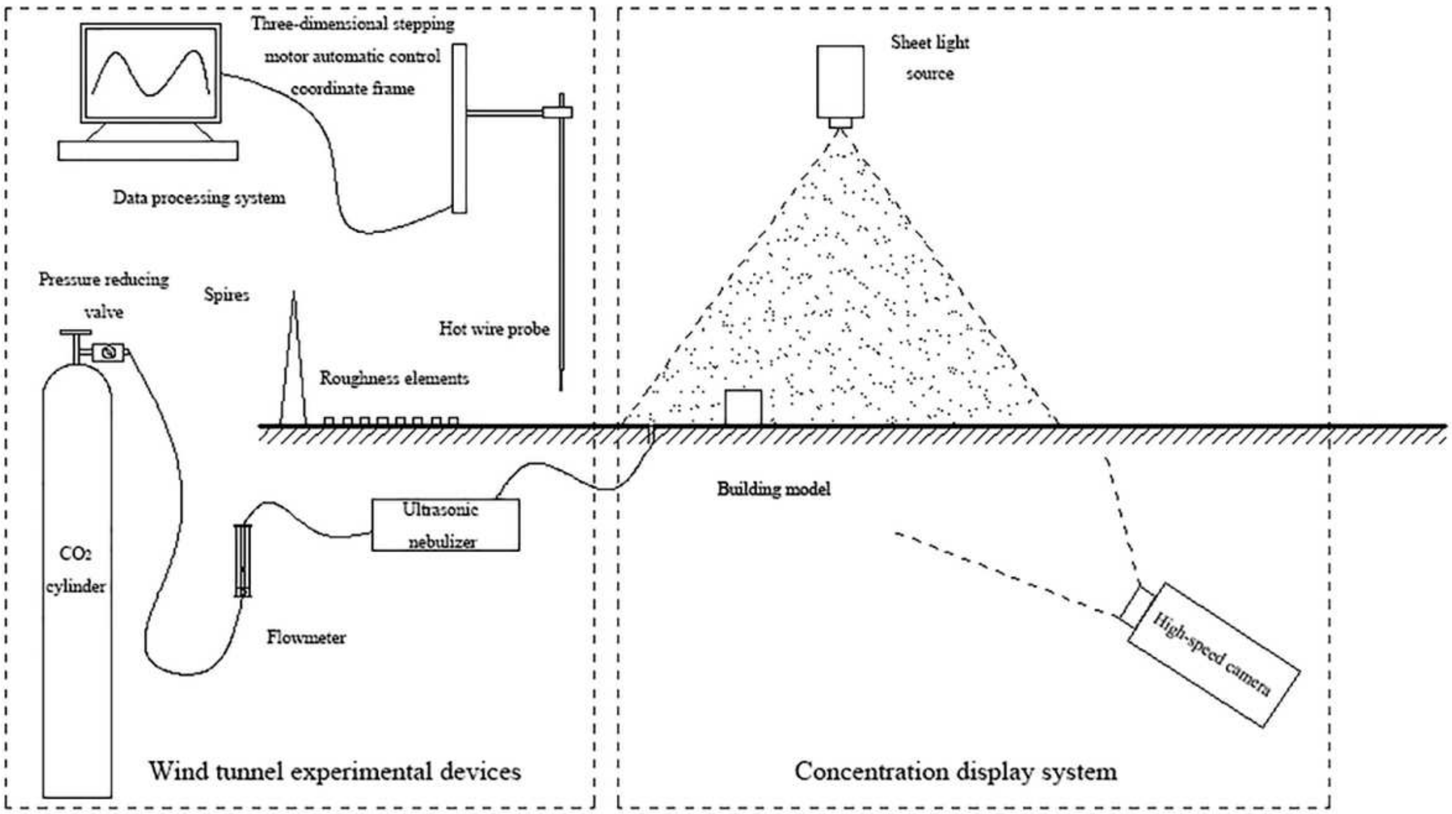

Figure 1

Experimental devices.

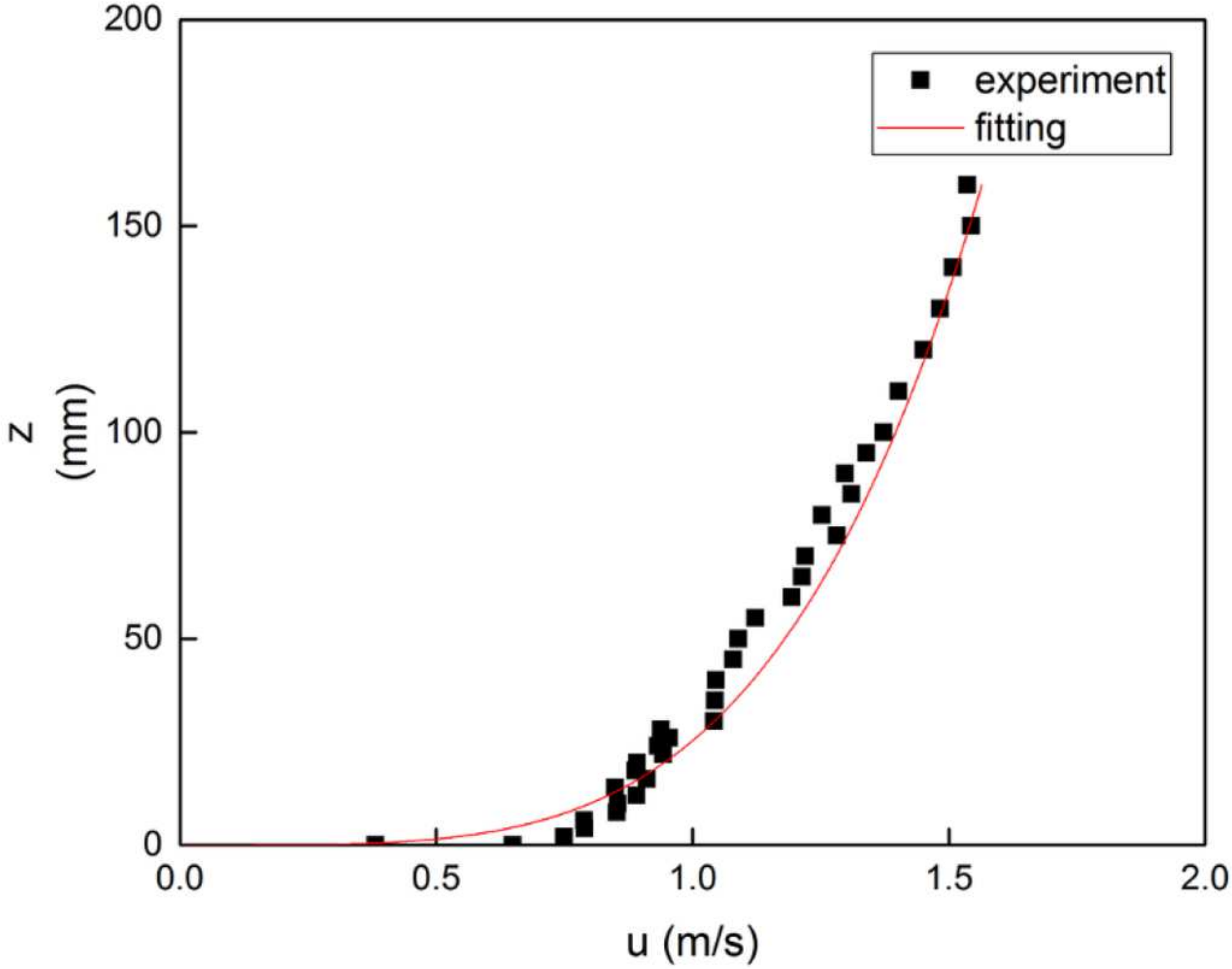

Figure 2

Experimental wind speed and fitting result.

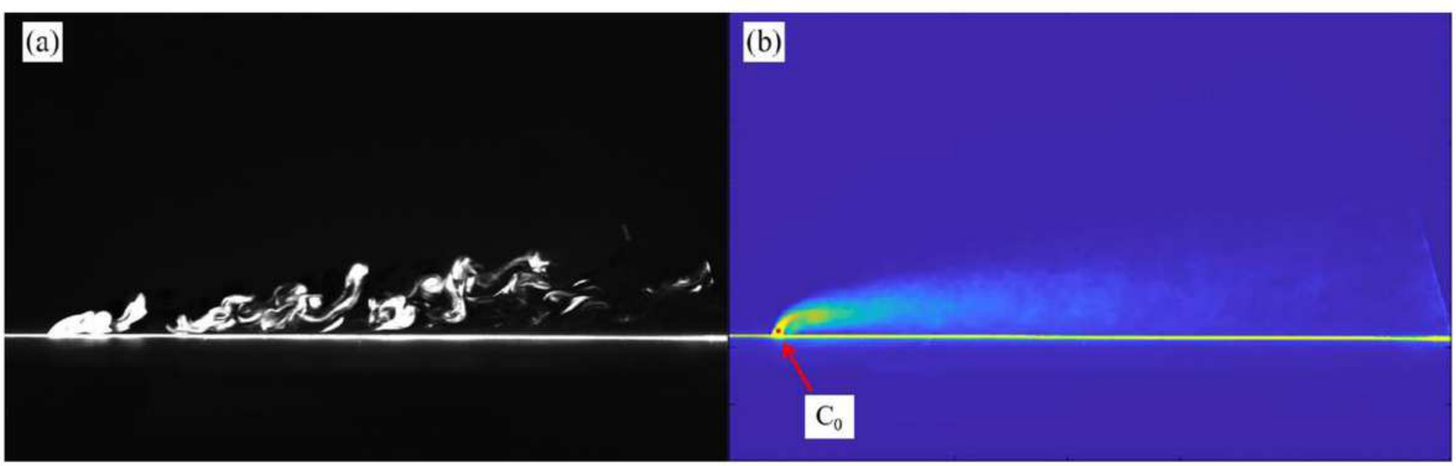

Figure 3

Pictures of (a) the instantaneous concentration field and (b) the time-average concentration field obtained in experiments.

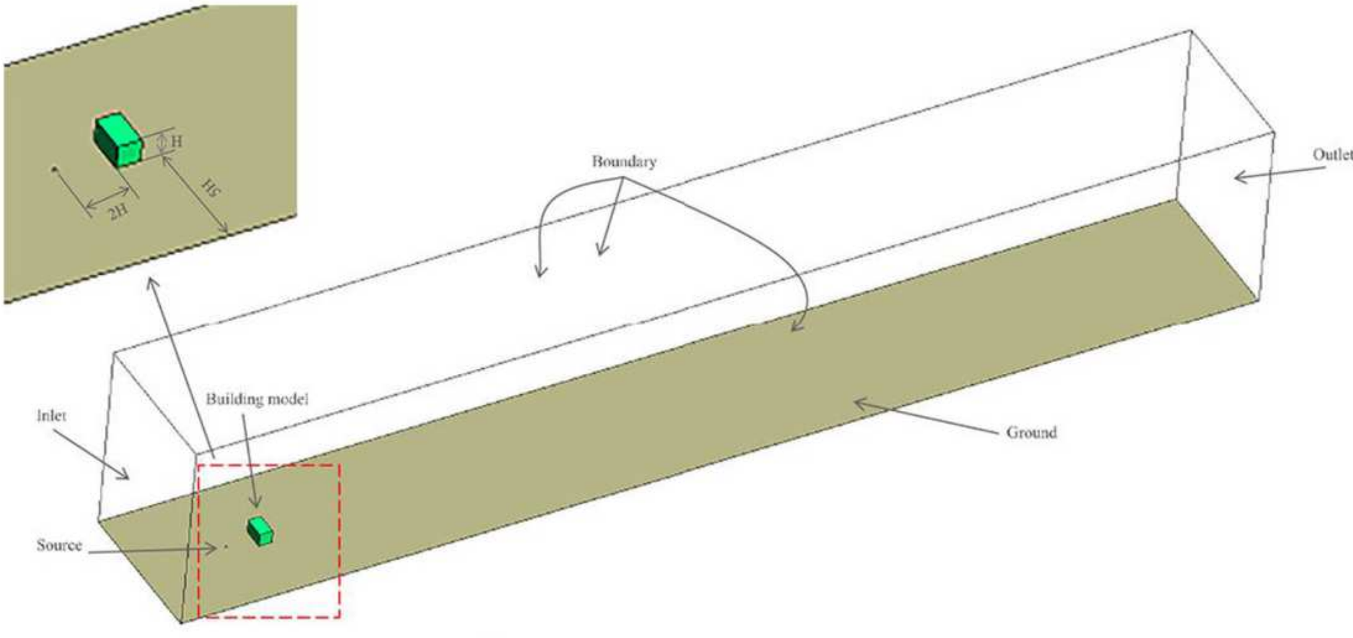

Figure 4

Domain and boundary of numerical simulation.

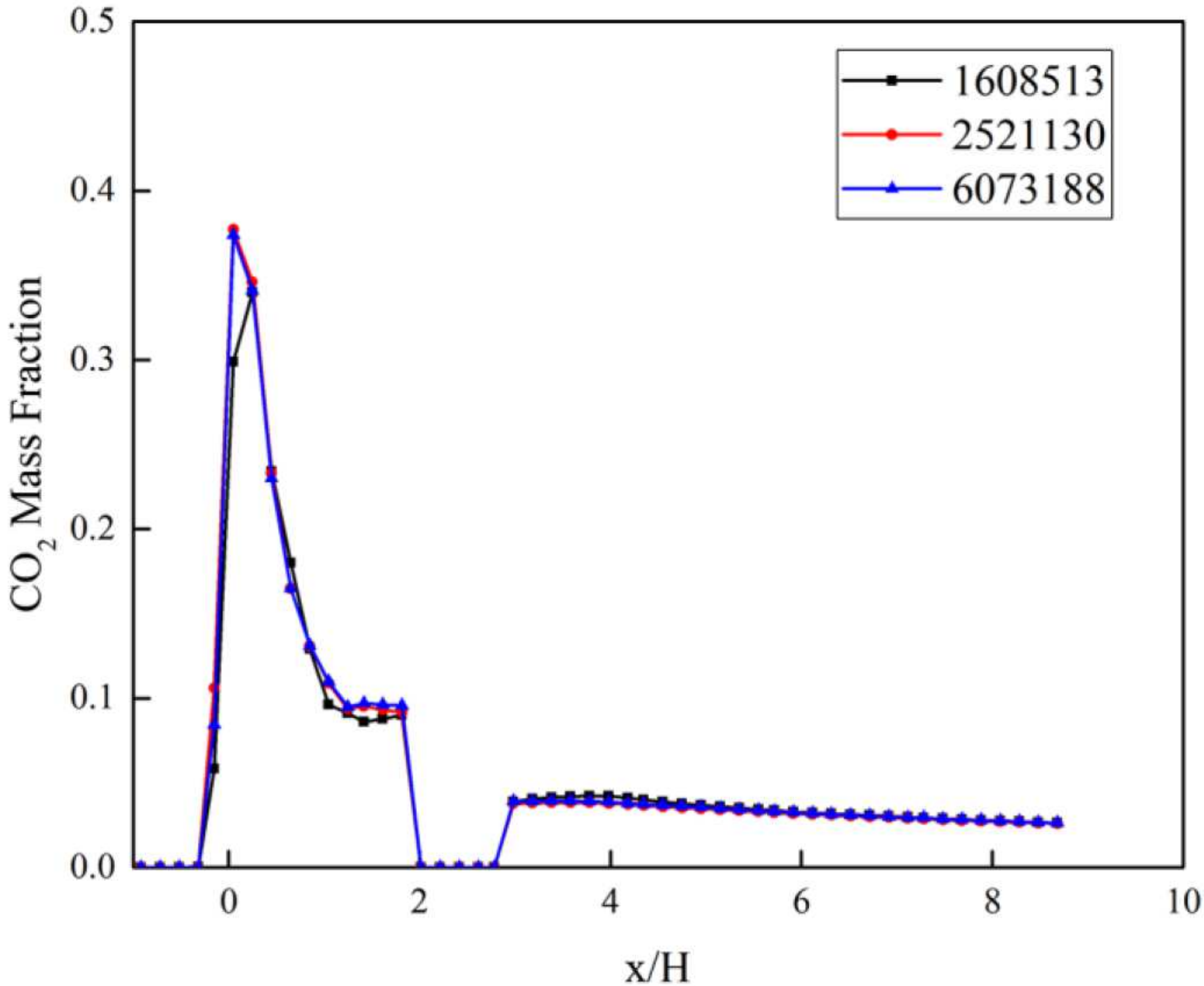

Figure 5

Grid independent verification.

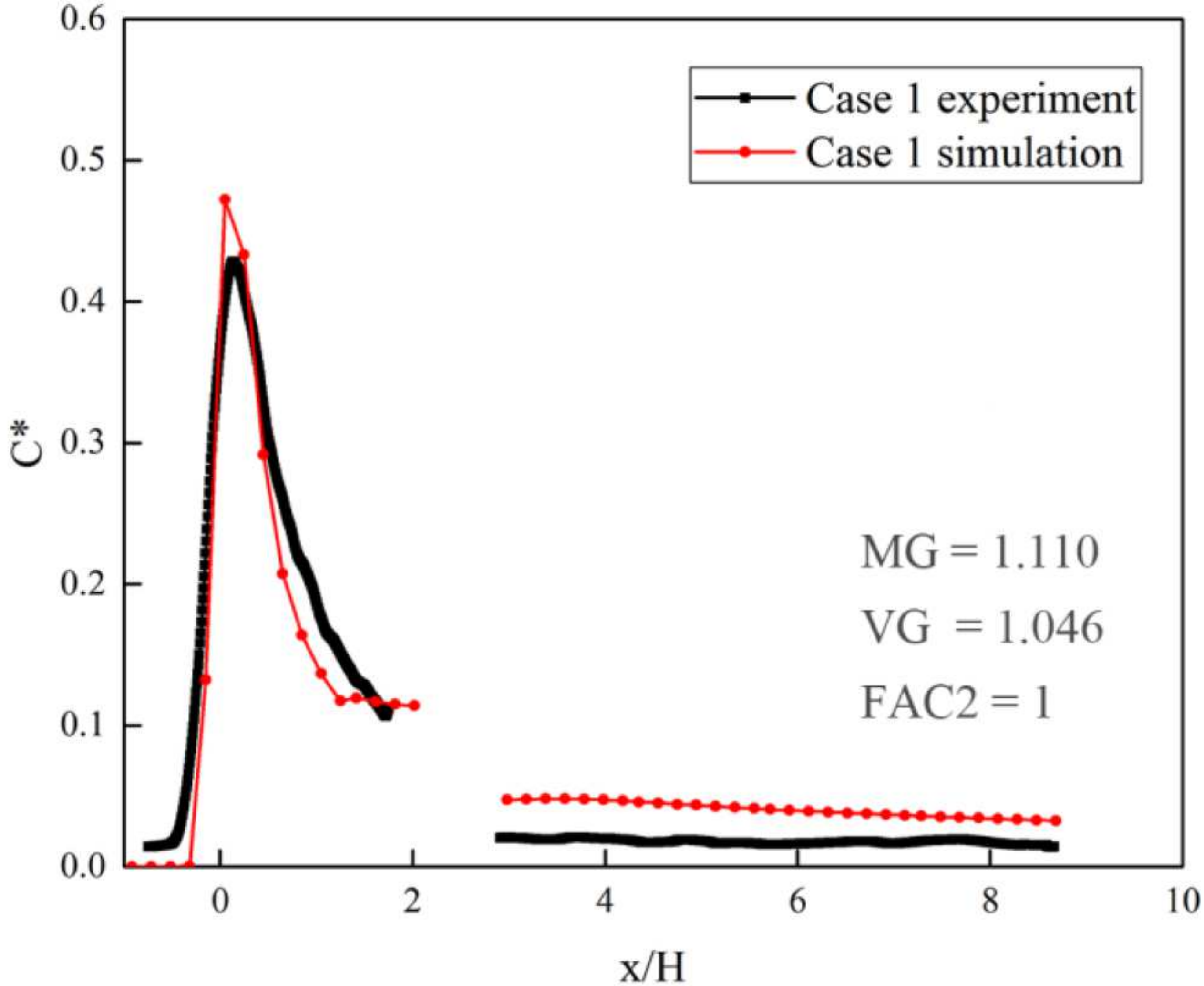

Figure 6

Comparison of simulation and experimental results for Case 1.

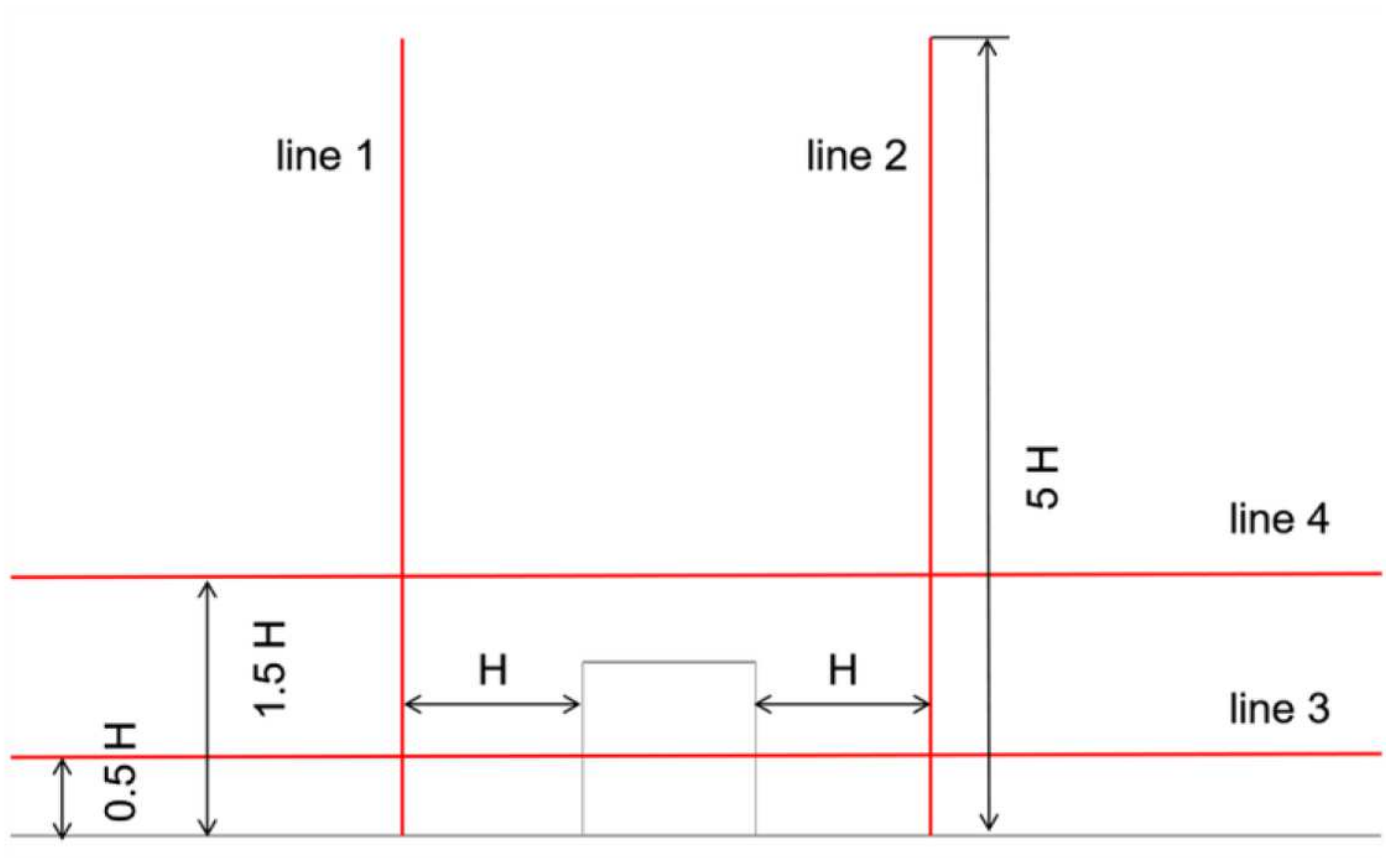

Figure 7

Monitoring lines for wind speed (line 1 and line 2) and pollutant concentration (line 3 and line 4).

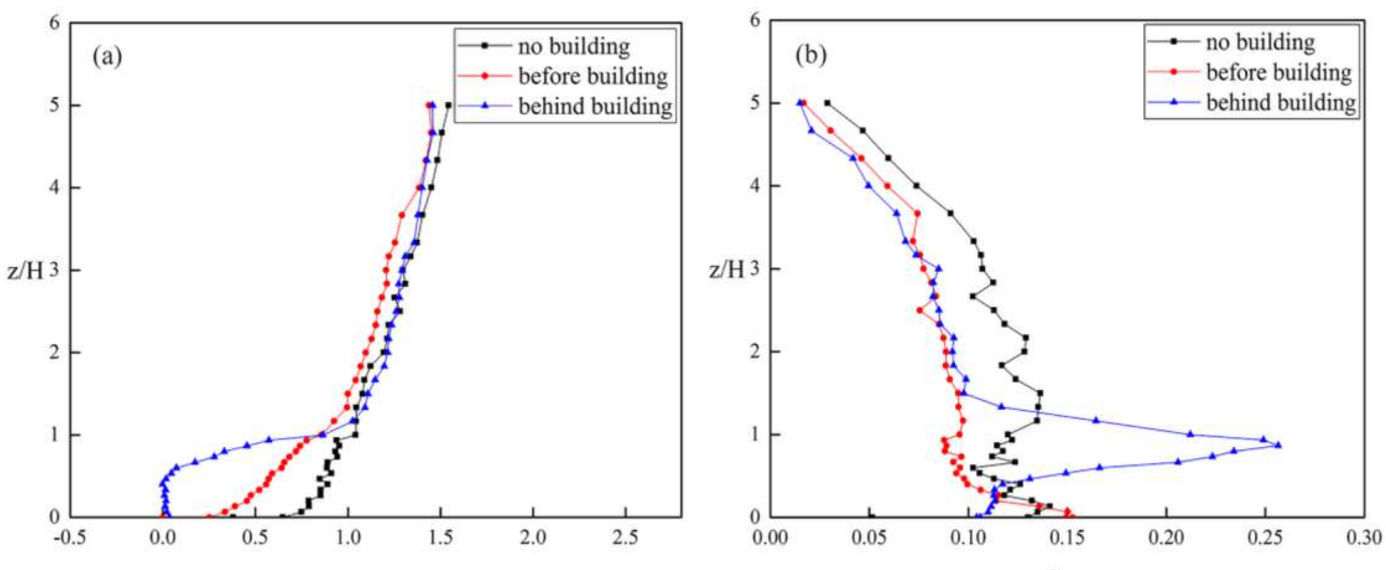

Figure 8

Distribution of (a) wind speed and (b) turbulence intensity at line 1 and line 2 in Case 1.

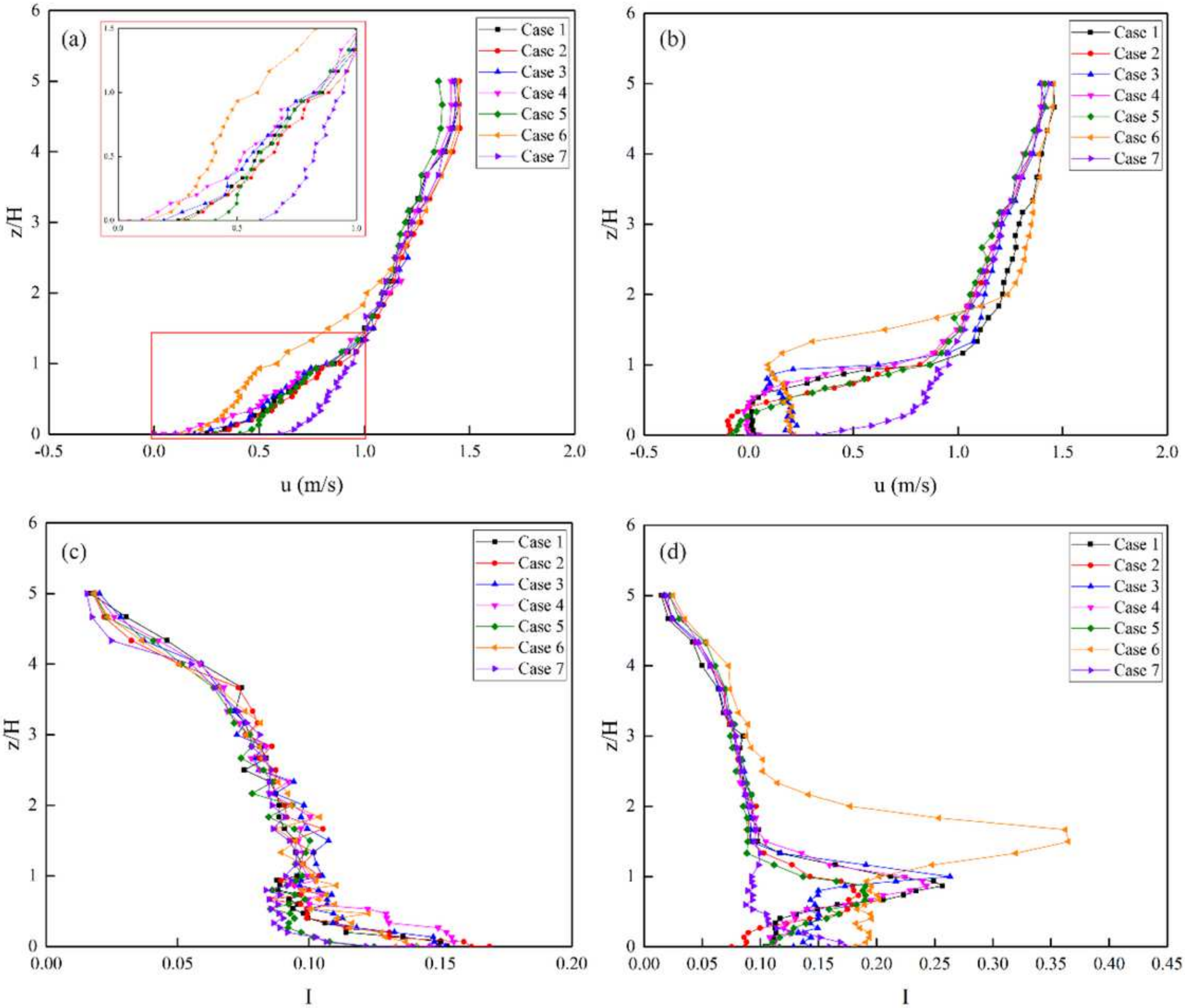

Figure 9

The wind speed (a, b) and the turbulence intensity (c, d) at line 1 and line 2 of the building under different conditions.

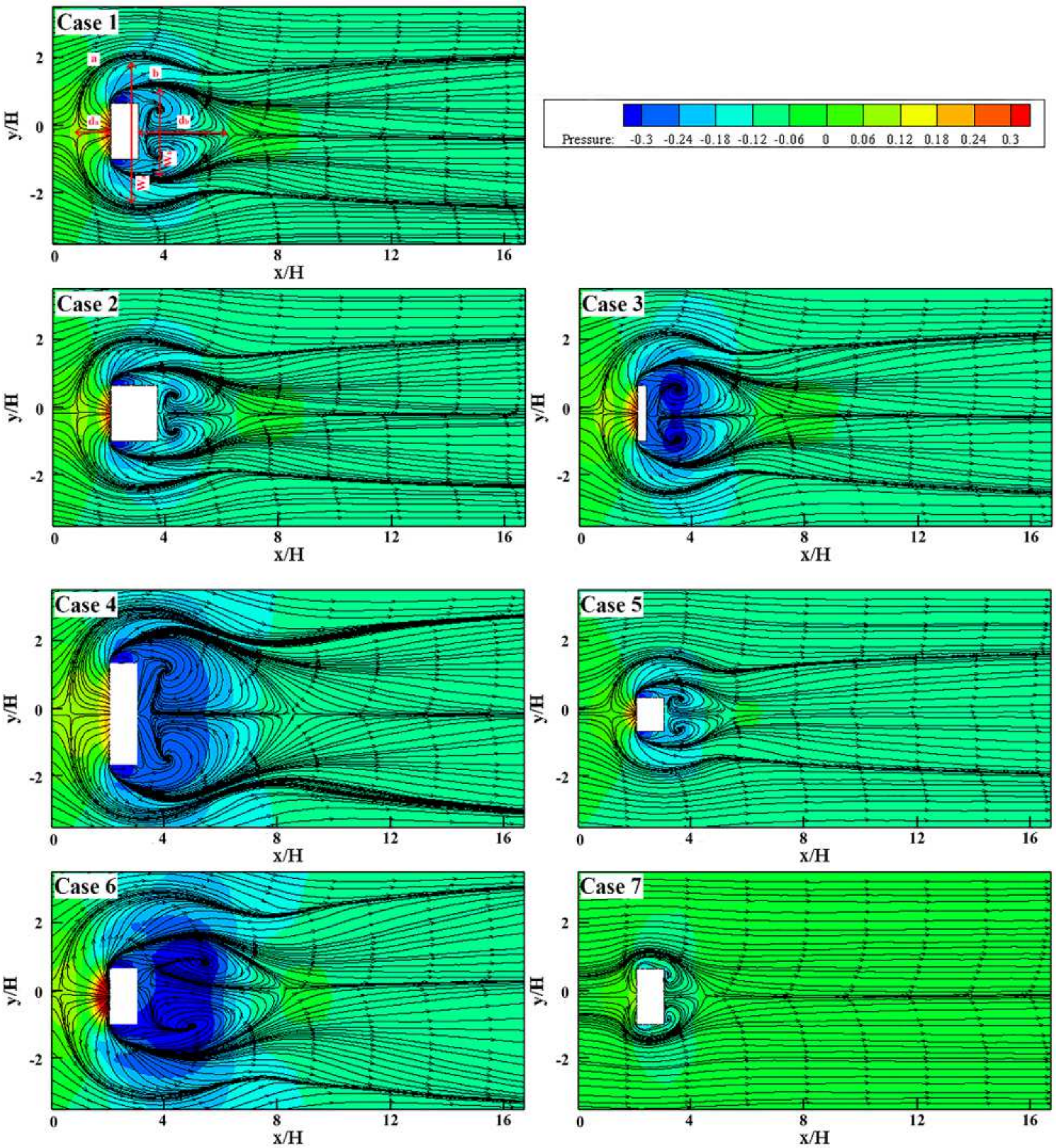

Figure 10

Time-averaged streamline and pressure contour of the horizontal plane of the ground (z=0) obtained by simulation.

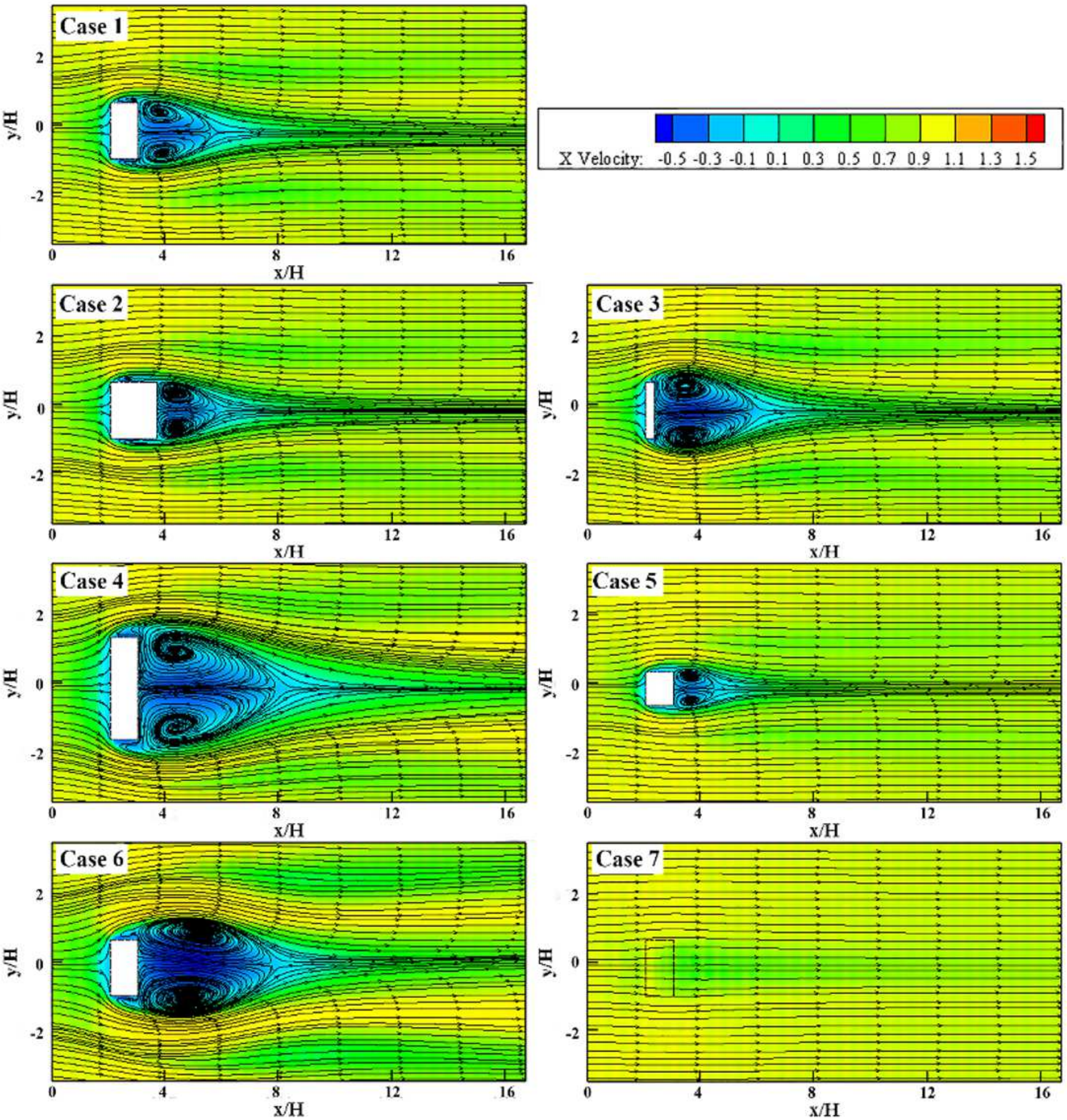

Figure 11

Time-averaged streamline and flow velocity counter of the horizontal plane (z/H=0.5) obtained by simulation.

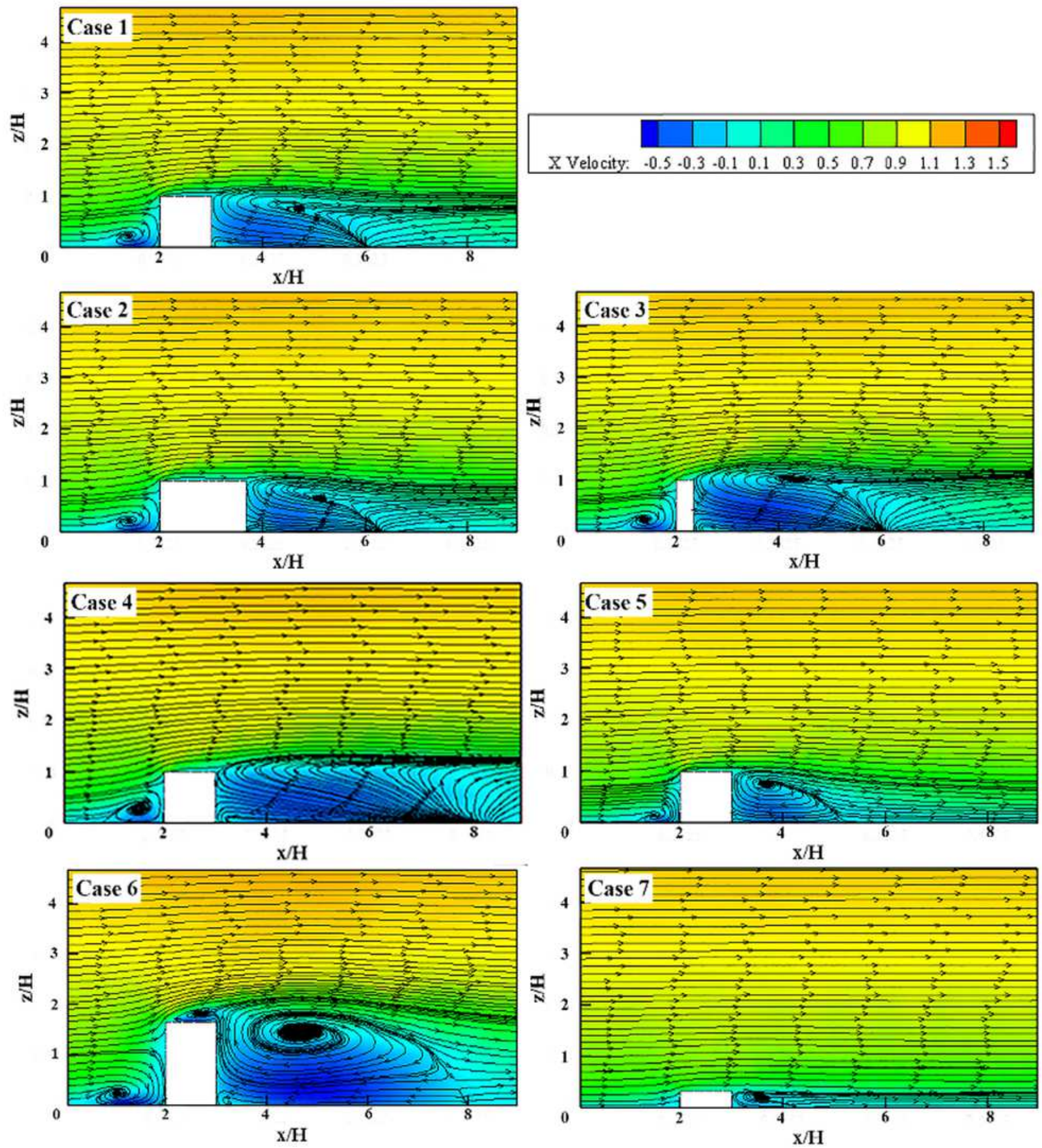

Figure 12

Time-averaged streamline and flow velocity counter of the vertical plane (y=0) in the middle of the building obtained by simulation.

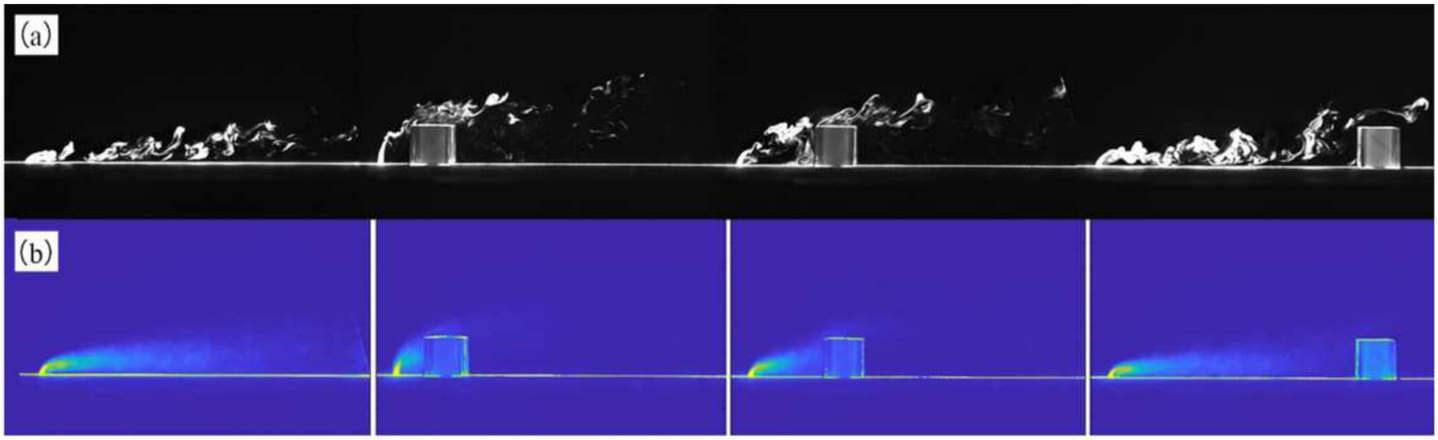

Figure 13

Results of the experiments with different distance between the building and the release source (no building, H, 2 H and 6.5 H): (a) instantaneous concentration field; (b) time-averaged concentration field.

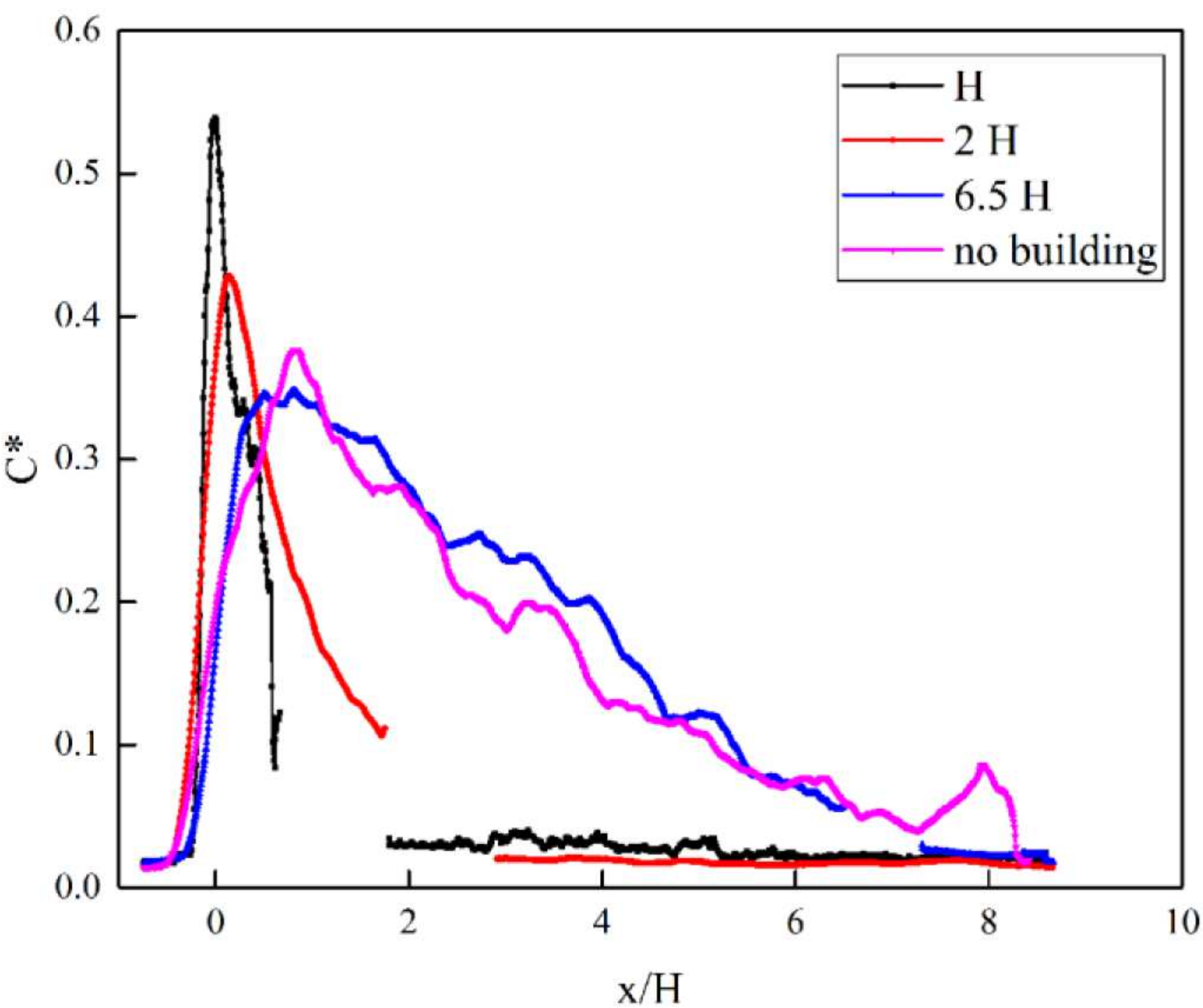

Figure 14

Concentration distribution curves on line 3 of the experiments with different distance between the building and the release source.

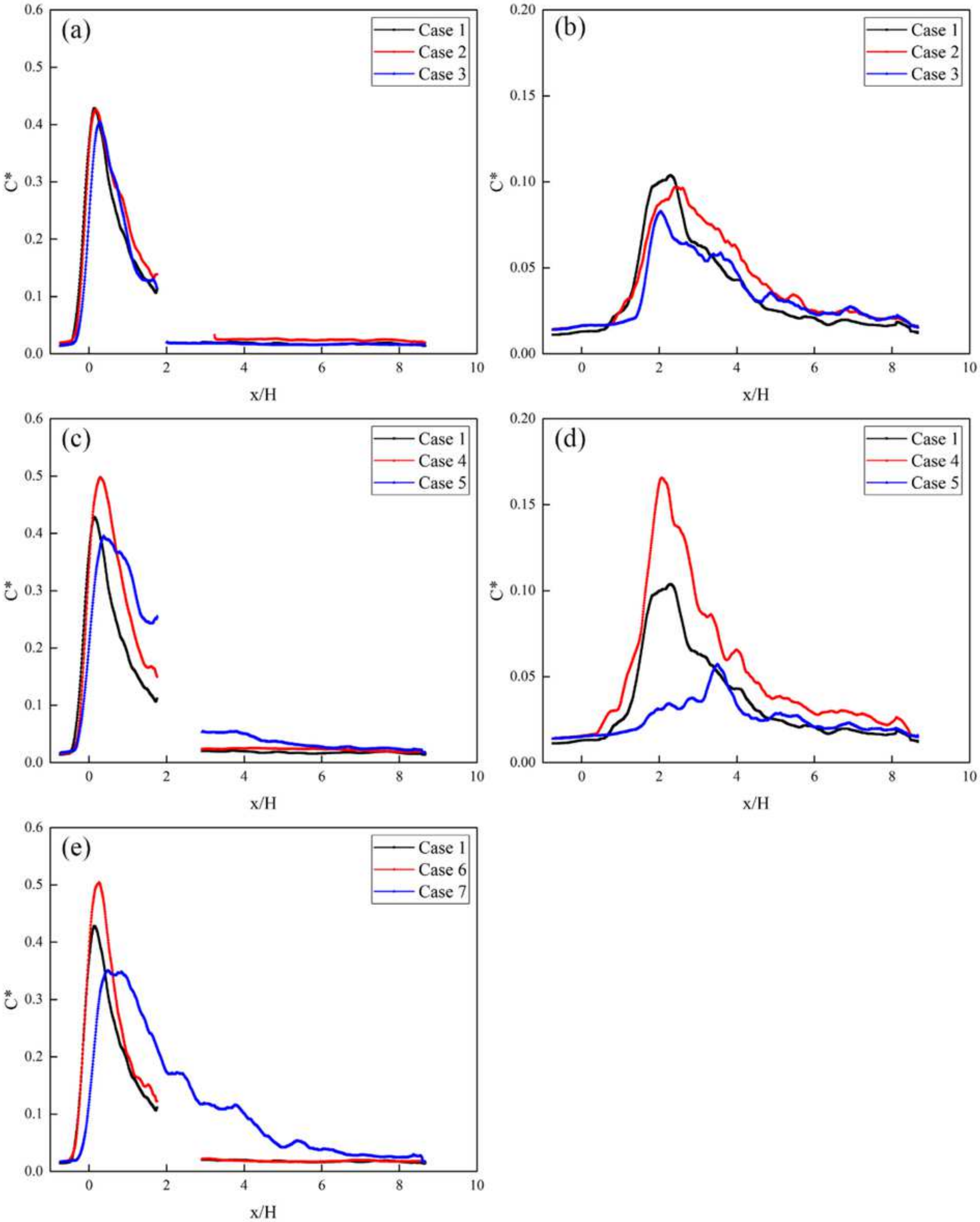

Figure 15

Concentration distribution curve of line 3 (a, c, e) or line 4 (b, d) in the experiments with different building size.

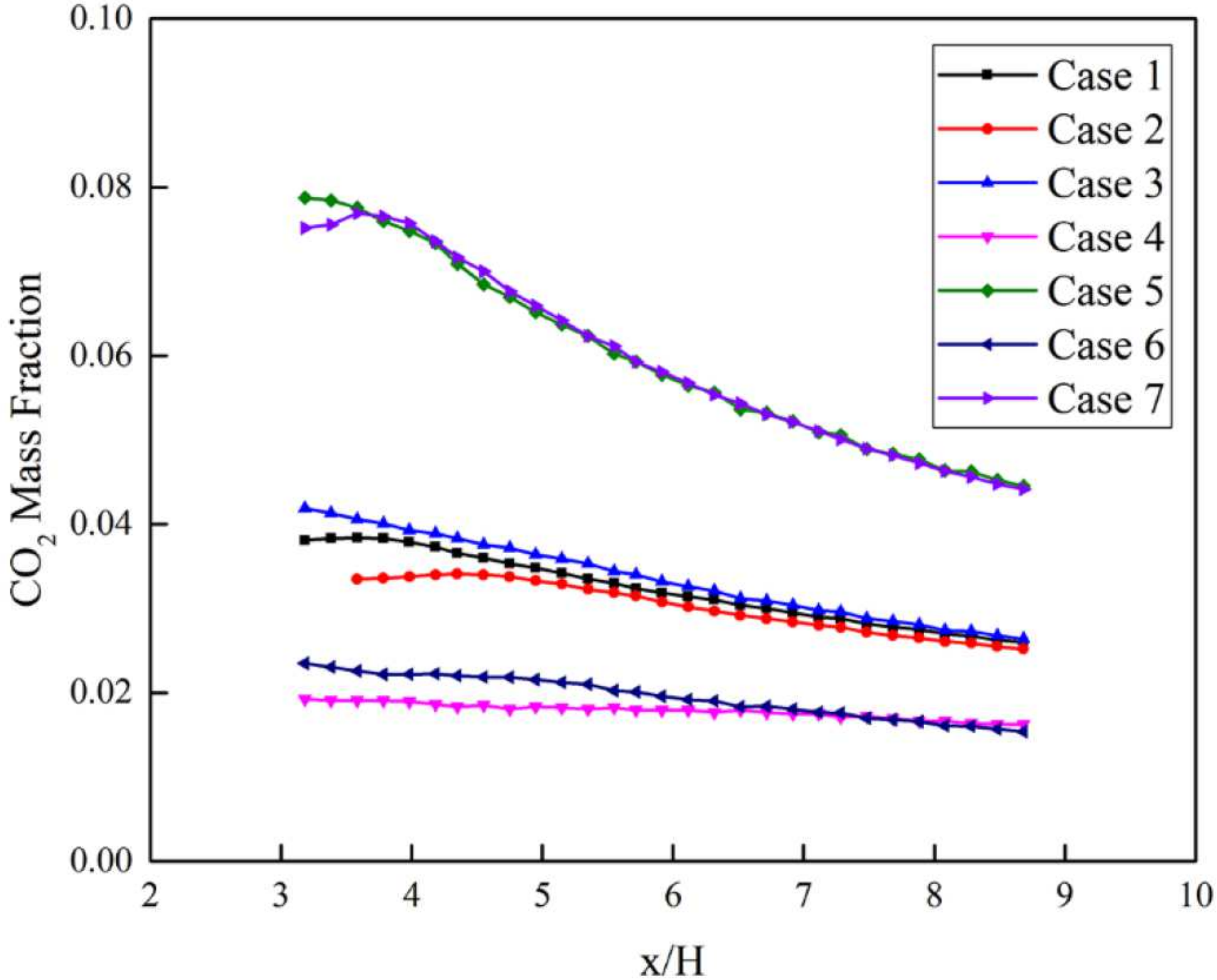

Figure 16

Pollutant concentration distribution on the leeward side obtained by simulation.